ELECTRICAL AND STRUCTURAL CHARACTERIZATION OF BISMUTH THIN FILMS

A THESIS SUBMITTED TO
THE GRADUATE SCHOOL OF NATURAL AND APPLIED SCIENCES
OF
MIDDLE EAST TECHNICAL UNIVERSITY

By

GÖKSEL DURKAYA

IN PARTIAL FULFILLMENT OF THE REQUIREMENTS
FOR
THE DEGREE OF MASTER OF SCIENCE
IN
PHYSICS

JULY, 2005

Approval of the Graduate School of Natural and Applied Sciences

_____

(Prof. Dr. Canan Özgen)
Director

I certify that this thesis satisfies all the requirements as a thesis for the degree of Master of Science.

_____

(Prof. Dr. Sinan Bilikmen)
Head of Department

This is to certify that we have read this thesis and that in our opinion it is fully adequate, in scope and quality, as a thesis for the degree of Master of Science.

_____

(Prof. Dr. Mehmet Parlak)
Supervisor

Examining Committee Members

Prof. Dr. Bülent Akınoğlu   (METU,PHYS)   _____

Assoc. Prof. Dr. Enver Bulur   (METU,PHYS)   _____

Assoc. Prof. Dr. Akif Esendemir   (METU,PHYS)   _____

Prof. Dr. Mehmet Çakmak   (GU,PHYS)   _____

Prof. Dr. Mehmet Parlak   (METU,PHYS)   _____

I hereby declare that all information in this document has been obtained and presented in accordance with academic rules and ethical conduct. I also declare that, as required by these rules and conduct, I have fully cited and referenced all material and results that are not original to this work.

Name, Last name : Göksel Durkaya

Signature   :

ABSTRACT

ELECTRICAL AND STRUCTURAL CHARACTERIZATION OF BISMUTH THIN FILMS

Durkaya, Göksel

M.S., Department of Physics

Supervisor: Prof. Dr. Mehmet Parlak

July, 2005, 58 pages

Electrical and structural properties of Bismuth thin films were studied simultaneously. Electrical properties of the Bismuth thin films have been characterized by measuring temperature dependent conductivity and Hall effect. Structural analysis were carried out by X-ray diffraction technique and using a room temperature Atomic Force Microscope (RT-AFM).

<u>Keywords</u>: Bismuth, Thin film, Thermal evaporation, Hall effect, Thermal annealing, XRD, Atomic Force Microscope (AFM).

ÖZ

BİZMUT İNCE FİLMLERİN
ELEKTRİKSEL VE YAPISAL KARAKTERİZASYONU

Durkaya, Göksel

Yüksek Lisans, Fizik Bölümü

Tez Yöneticisi: Prof. Dr. Mehmet Parlak

Temmuz, 2005, 58 sayfa

Bizmut ince filmlerin elektriksel ve yapısal özellikleri eşzamanlı incelendi. Elektriksel özelliklerin karakterizasyonu için Hall etkisi ölçümleri yapıldı. Kristal yapı X ışını kırınım spektrumu kullanılarak takip edildi ve yüzey topografisi incelemesi için Oda Sıcaklığı Atomik Kuvvet Mikroskobu (OS-AKM) kullanıldı.

Anahtar Kelimeler: Bizmut, İnce film, Isısal Buharlaştırma, Hall etkisi, Isıl Tavlama, X ışını girişimi (XRD), Atomik Kuvvet Mikroskobu (AKM).

Babam balık tuttu, annem pişirdi,

hep beraber yedik.

ACKNOWLEDGEMENTS

TABLE OF CONTENTS

LIST OF FIGURES

FIGURES

LIST OF TABLES

TABLES

CHAPTER 1

Introduction

In this chapter, general properties and usage of bismuth metal are described. The theoretical basis of Hall effect is presented. Electrical properties of semiconductors and their temperature dependence are described. The polycrystalline structure is a subject for grain boundary theory which is covered by this section. Finally, a method for surface studies, Atomic Force Microscopy (AFM) and the methods in AFM and why we choose Quartz Tuning Fork Atomic Force Microscope (QTF-AFM) are described.

1.1 What is Bismuth?
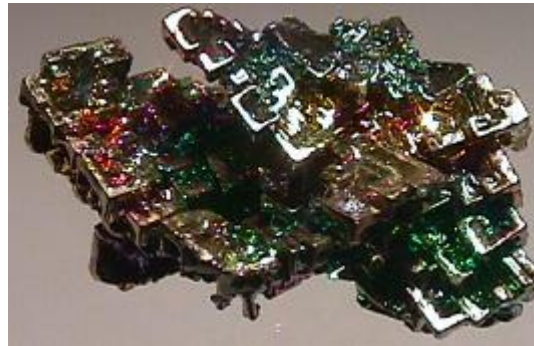
Figure 1.1: Picture of Bismuth ore

Bismuth is a metal belonging into the fifth main group of the periodic system of chemical elements, where you will find nitrogen, phosphor, arsenic, antimony and bismuth. Bismuth has a Rhombohedral crystal structure ($\alpha,\beta,\gamma \neq 90^{o}$). Bismuth is rarely found in nature in its elemental form. Only 0.008 ppm (grams per metric ton) of the earths crust consists of bismuth which is less than for platinum which ranks number 68 with 0.01 ppm. It melts at 271°C, expands by 3.32% on solidification, and boils at 1560°C. It has the lowest thermal conductivity of all metals, except mercury, while its electrical conductivity is greater in the solid than

1

in the liquid state. It has a small effective electron mass, long carrier mean free path[1].
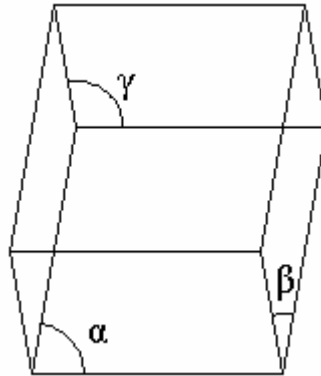
Figure 1.2: Rhombohedral crystal structure ($\alpha,\beta,\gamma{\neq}90^{\circ}$C)

Bismuth has a very interesting property: Similar to water, instead of contracting when it solidifies, like all other matter, it expands. This, and the fact that it is very diamagnetic, offers it numerous uses in the electronic field. Quite interestingly for a heavy metal indeed, the international scientific community recognizes that bismuth is one of the safest elements and it currently has a growing number of industrial and medical applications depending upon it to alleviate specific toxicity or environmental problems. Main uses of bismuth in industry are in pharmaceuticals, low melting point alloys, fuses, sprinklers, glass, ceramics and as a catalyst in rubber production. On the other hand, metallic single-crystal bismuth has an extremely high magnetoresistance [2],[3] giving rise to the potential for creating very good magnetic field sensors. Such metallic forms of bismuth will typically demonstrate a resistance that decreases by two orders of magnitude when cooled to liquid helium temperatures (~5 K). They also exhibit semiconductor effects on their oxides [4,5]. The growth of high-quality metallic thin films of bismuth, however, has proven to be very difficult.

1.1.1 Magnetoresistance

Magnetoresistance refers to an increase in the resistance when the sample is

subjected to an magnetic field. The physical explanation is that when a magnetic field is applied, the trajectories of electrons between collisions will acquire a curvature. This means that the component of motion in the direction of the applied electric field will be reduced by the presence of the magnetic field, and therefore the resistance will be higher.

1.2 Hall Effect

If an electric current flows through a conductor in a magnetic field which is perpendicular to the plane of the electric current, the charge carriers are subjected to a transverse force which tends to push the charge carriers to one side of the conductor. This is the most evident in a thin flat conductor as illustrated in Fig.1.3. A buildup of charge at the sides of the conductors will balance this magnetic influence, producing a measurable voltage between the two sides of the conductor. The presence of this measurable transverse voltage is called the Hall effect after E. H. Hall who discovered it in 1879 [6].
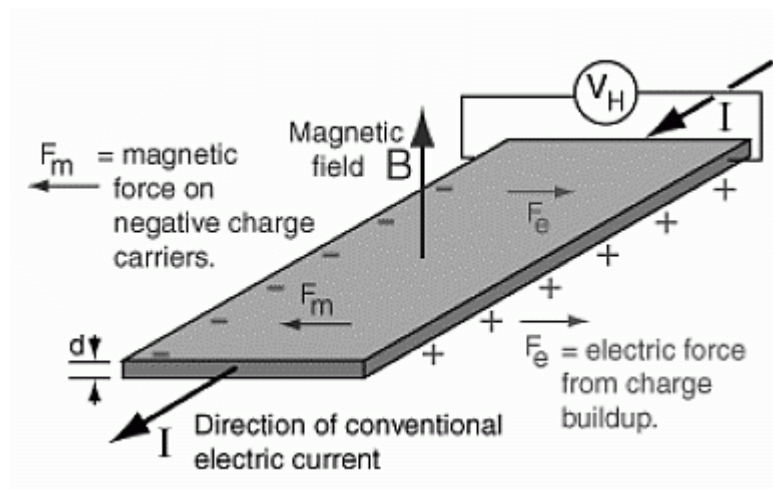
Figure 1.3: Scheme for a current carrying flat conductor under magnetic field

The Hall effect is analogous to the magnetic detection of an electron beam in a cathode ray tube. The physical principle is the well known Lorenz force,

$$\vec{F} = q \, \vec{v} \times \vec{B} \tag{1.1}$$

3

acting on a charged particle. When a charge carrier moves along a direction perpendicular to an applied magnetic field, it experiences a force, acting perpendicular to both directions and the charged particle moves in response to this force. This perpendicular force causes the carriers to accumulate towards one edge of the conductor. If the carriers are electrons, then the direction of motion is opposite to the direction of the conventional current flow and the magnetic force (F_m) acts as shown in Fig. 1.3. The accumulation of electrons creates and electric field that also becomes effective as an electric force on the carriers. Finally, an equilibrium establishes among the competing electric and magnetic forces. This equilibrium gives us:

$$\overrightarrow{F}_m = \overrightarrow{F}_E \qquad (1.2)$$

$$\overrightarrow{F}_E = q(\overrightarrow{v} \times \overrightarrow{B}) = q\,\overrightarrow{E} \qquad (1.3)$$

$$E = -v_d B \qquad (1.4)$$

The result can be interpreted in another way using the definition of microscopic current. If the total mobile charge moving with a drift velocity v_d along a conductor of length L is assumed to be Q, then,

$$Q = nwdLq \qquad (1.5)$$

where w, d, n are the width, thickness of the conductor and the free carrier density, respectively. The transition time to pass that length L of the material is

$$t = \frac{L}{v_d} \qquad (1.6)$$

and one gets the current I,

4

$$I = \frac{Q}{t} = \frac{dwnLq}{L/v_d} \tag{1.7}$$

$$I = dwnqv_d \tag{1.8}$$

Now, Eqn. 1.4 can be reformulated as,

$$E = -\frac{IB}{wdqn} = \frac{V_H}{w} \tag{1.9}$$

$$\Rightarrow V_H = -\frac{IB}{dqn} \tag{1.10}$$

$$R_H = -\frac{1}{nq} \tag{1.11}$$

$$V_H = \frac{IB}{d}R_H \tag{1.12}$$

where V_H is the Hall voltage built up across the conductor and R_H is the proportionality factor, known as the Hall coefficient.

The Hall effect is, therefore, a conduction phenomenon which is different for different charge carriers, so is the Hall voltage. In most common electrical applications, it makes no difference whether you consider positive or negative charge to be moving, but the Hall voltage and Hall coefficient have different polarity for positive and negative charge carriers namely for holes and electrons.

In an intrinsic semiconductor at temperatures above absolute zero, there will be some electrons, which are excited across the band gap into the conduction band and these can produce electric current. When the electron in semiconductor crosses the gap, it leaves behind an electron vacancy or hole in the regular lattice. Under the influence of an external voltage, both the electron and the hole can move across

the material, but in opposite direction. In an n-type semiconductor, the dopant contributes extra electrons, dramatically increasing the conductivity. In a p-type semiconductor, the dopant produces extra holes, which likewise increase the conductivity. Thus, depending on the material properties of the semiconductors being used, the sign of the voltage becomes either positive or negative. So, using this fact, unknown conduction properties of newly developed materials can be studied.

The Hall effect has gained an important place in the history of science and industry by providing accurate and easy measurement of carrier density and the mobility of carriers in semiconductors and metals.

1.3 Electrical Conductivity and Mobility in Semiconductors

For the electrical conduction in metals, ***Ohm's law*** is

$$I = \frac{V}{R} \tag{1.13}$$

where ***I*** is the current, ***V*** is the potential difference and ***R*** is the resistance between terminals where the measurement is done. And the respective equations are

$$J = \frac{I}{A} \ , \ E = \frac{V}{L} \ \text{ and } \ R = \frac{L.\rho}{A} \tag{1.14}$$

where ***J*** is the current density, ***A*** is the cross section, ***E*** is the electrical field, ***L*** is the length and ***ρ*** is the electrical resistivity which is the inverse of the electrical conductivity ***σ*** [7].

$$\sigma = \frac{1}{\rho} = \frac{L}{R.A} \tag{1.15}$$

By using Eqn.s (1.13), (1.14) and (1.15), we result that

$$J = \sigma.E \qquad (1.16)$$

The above equations gives us a conductivity with a dimension of order of m^{-1}. However, our concern is to work in microscopic dimensions.

To pass microscopic domain, let us be interested in the motion of an electron through lattice sites. When an electron moves through lattice sites, it is subjected to a friction force due to collisions. The field due to *V*, exerts a force *– eE* on the electron. Using Newton's law [8]

$$m*.\frac{dv}{dt} = -e.E - m*.\frac{v}{\tau} \qquad (1.17)$$

where *–m*v/τ* represents the friction force, *m** is the effective mass, *τ* is the collision time.

For steady-state velocity of the electron, *dv/dt = 0*. Then, the steady state velocity of the electron,

$$\upsilon = -\frac{e.\tau}{m*}E \qquad (1.18)$$

which is opposite to *E*, because of negative charge on the electron.

The solution (Eqn. (1.18)) is for drift velocity v_d, although a random velocity v_r is still present which is due to random motion of the electron.

The current density *J* can be calculated from Eqn. (1.16). There is a charge *–ne* per unit volume where *n* is the charge concentration. Then

7

$$J = (-n.e)v_d = (-n.e)(-\frac{e.\tau}{m*}E) = \frac{ne^2\tau}{m*}E \qquad (1.19)$$

From Eqn. (1.16), since the electrons are represented by an effective mass m_e^*,

$$\sigma_e = \frac{ne^2\tau_e}{m_e^*} \qquad (1.21)$$

where τ_e is the lifetime for the electron. As understood from Eqn. (1.21) σ_e is small in semiconductors where n is low and it is high for metals where n is higher. The typical electrical conductivity σ_e values for semiconductors are about 10^{21} m^{-3} and for metals 10^{28} m^{-3} [9].

For electrical transport characterization, another coefficient named mobility μ is used. Mobility is a measure of the rapidity, or swiftness, of the motion of the electron in the field which is the ratio of the drift velocity v_e to applied electric field E [10] .

$$\mu_e = \frac{v_e}{E} \qquad (1.22)$$

By inserting Eqn. (1.18) into Eqn. (1.22)

$$\mu_e = \frac{e\tau_e}{m_e^*} \qquad (1.23)$$

By using Eqn. (1.21) and Eqn. (1.23), we can express σ in terms of μ

$$\sigma_e = ne\mu_e \qquad (1.24)$$

The lifetime τ is temperature dependent, therefore the mobility μ and then the conductivity σ depends on temperature.

1.3.1 Temperature Dependence of Conductivity

For temperature dependence, one should use Fermi-Dirac distribution function [11].

$$f(E) = \frac{1}{e^{(E-E_F)/k_BT} + 1} \tag{1.25}$$
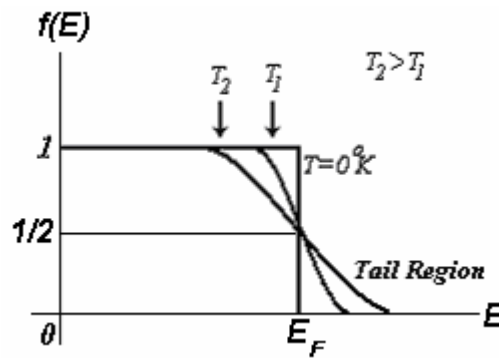
Figure 1.4: Fermi-Dirac distribution

As seen in Fig. 1.4, as the temperature rises, the higher energy states which are beyond Fermi level E_F start to be occupied more as the states below Fermi level get unoccupied. The tail region in Fig.1.4 is the particular interest for semiconductors where $(E-E_F) >> k_BT$. So (1.25) reduces to

$$f(E) = e^{E_F/k_BT} e^{-E/k_BT} \tag{1.26}$$

The concentration of electrons in conduction band which entirely lies on tail region is given as

$$n = \int_{E_{c1}}^{E_{c2}} f(E) g_e(E) dE \tag{1.27}$$

where

9

$$g_e(E) = \frac{1}{2\pi^2}\left(\frac{2m_e^*}{\hbar^2}\right)^{3/2}\left(E - E_g\right)^{1/2} \tag{1.28}$$

$g_e(E)dE$ is the number of electrons found in the energy range *(E* and *E+dE)*, *f(E)* is the occupation probability, E_{c1} and E_{c2} are the bottom and top of the band respectively.

By solving Eqn. (1.27) by changing the variables, we get

$$n = 2\left(\frac{m_e^* k_B T}{2\pi\hbar^2}\right)^{3/2} e^{E_F/k_B T} e^{-E_g/k_B T} \tag{1.29}$$

The same procedure gives the concentration of holes *p* as;

$$p = 2\left(\frac{m_h^* k_B T}{2\pi\hbar^2}\right)^{3/2} e^{-E_F/k_B T} \tag{1.30}$$

We know that n and p are equal to each other because each hole corresponds to an electron vacancy. If we equate Eqn. (1.29) and Eqn. (1.30) to each other, E_F becomes

$$E_F = \frac{1}{2}E_g + \frac{3}{4}k_B T \log\left(\frac{m_h^*}{m_e^*}\right) \tag{1.31}$$

The assumption $E_g \gg k_B T$ [9] results that the energy level is close to the middle of the energy gap. If we combine Eqn. (1.29) and Eqn. (1.31), the electron concentration becomes

$$n = 2 \left(\frac{m_e^* k_B T}{2\pi \hbar^2} \right)^{3/2} (m_e^* m_h^*)^{3/4} e^{-E_g/2k_B T} \qquad (1.32)$$

The mobility μ has two components for electrons and holes as μ_e and μ_h. Then, the conductivity becomes

$$\sigma = ne\mu_e + pe\mu_e \qquad (1.33)$$

$$n = p \Rightarrow \sigma = ne(\mu_e + \mu_h) \qquad (1.34)$$

If we combine Eqn. (1.32) and Eqn. (1.34), we may write σ as;

$$\sigma = f(T)e^{-E_g/2k_B T} \qquad (1.35)$$

where $f(T)$ is a function which depends only weakly on the temperature. The most important result of Eqn. (1.35) is that the activation energy E_g can easily be calculated by using the equation

$$\log \sigma = \log f(T) - \frac{E_g}{2k_B} \frac{1}{T} \qquad (1.36)$$

The slope of the $log\sigma$ vs $1/T$ graph gives $-E_g/2k_B$ values in different temperature regions.

1.3.2 Temperature Dependence of Mobility

Mobility is given in terms of lifetime as;

$$\mu_e = \frac{e\tau_e}{m_e^*} \qquad (1.37)$$

11

$$\tau_e = \frac{l_e}{v_r} \tag{1.38}$$

where l_e is the mean free path of the electron [12,1] and v_r is its random velocity. The collision time τ is high for Bismuth. Because it has a long mean-free-path [2]. It might be better to write the collision time as;

$$\bar{\tau}_e = \frac{l_e}{\bar{v}_r} \tag{1.39}$$

where we used average signs to indicate that we somehow averaged the random motion over all electrons to reach a behavior for all system.

Then, we may write mobility as;

$$\mu_e = \frac{e l_e}{m_e^* \bar{v}_r} \tag{1.40}$$

Using the kinetic theory of gases [29]

$$\frac{1}{2} m_e^* \bar{v}_r^{\,2} = \frac{3}{2} k_B T \tag{1.41}$$

Then, Eqn. (1.40) takes the following form

$$\mu_e = \frac{e l_e}{(m_e^*)^{1/2} (3 k_B T)^{1/2}} \tag{1.42}$$

So that the mobility depends on $T^{-1/2}$. The mean free path l_e does also have temperature dependence just as it does in metals. At high temperatures, collision with phonons (lattice scattering) starts to be dominant and l_e becomes inversely

12

proportional to temperature so that $\mu_e \sim T^{-3/2}$ [13]. If ionized impurity scattering is dominant, generally in low temperatures, then, $\mu_l \sim T^{+3/2}$. If both are present, the reciprocal of the effective total bulk crystalline mobility is the sum of reciprocals of the mobilities of both mechanisms [14].

1.4 Grain Boundary Theory

When talking about the electrical properties of the thin films, we know that those properties are affected by the changes in the internal structures of the thin films. Those changes in the internal structures of a polycrystalline structure are due to the growth mechanisms of the grains.

When a solid forms from the liquid it does so by nucleation and the growth of small crystallites randomly oriented throughout the solidifying system, and these islands grow as the liquid solidifies. This is what happens in thermal evaporation growth. The temperature of the substrate is also important in the process because the hotter substrate mainly helps the system to get close to the lower energy state producing better crystalline structure. The tendency to reach the lower energy state of a system results with different crystal structures according to the nature of the atom. Same material may also exhibit different structures depending upon the growing conditions [15]. The crystals continue to grow until they meet with neighbouring and, in general, the individual crystals will not be either of the same orientation or aligned. The boundary where they meet called the grain boundary becomes a surface and the mismatch in orientation is accomodated by distortion and gaps in the atomic arrangement. For an ideal system, the grain shape, size and distribution aim to minimise the surface energy and thus reduce the surface area. The ideal shape will minimise the energy for a grain of a given size, but simply increasing the grain size or decreasing the number of grains will reduce the grain boundary area and hence the total surface energy. Grains therefore tend to grow with time, but for this to occur the atoms must be able to migrate from one grain to the next across grain boundary. This can only occur at relatively high temperatures, typically greater than half the melting point. The rate of grain growth will increase with increasing temperature, and the mobility of a grain boundary, μ, takes the

form [16]

$$\mu = \mu_0 e^{-E_a / kT} \tag{1.43}$$

where μ_0 is a constant, E_a is the grain boundary potential energy. Eqn. (2.1) shows that grain growth is an exponential function of temperature.

1.5 Atomic Force Microscopy

Atomic Force Microscopy [17] was invented by Binnig, Quate and Gerber in 1986 as a tool for studying insulating and conducting surfaces. Basic principle of an Atomic Force Microscopy theory is shown in Fig. 1.5.
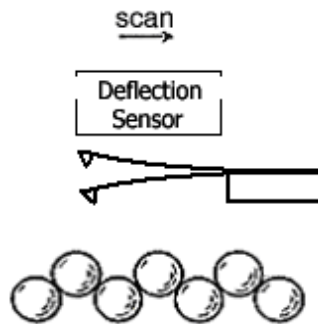
Figure 1.5: Scheme for an Atomic Force Microscope

In fact, the concept of using a force to image a surface is a general one, and can be applied to magnetic and electrostatic forces as well as the interatomic interaction between the tip and the sample. Whatever the origin of the force, all force microscopes have five essential components [18] :

- A sharp tip integrated to a cantilever spring;

- A way of sensing the cantilever deflection;

- A feedback system to monitor an the deflection (and, hence, the interaction force);

- A mechanical scanning system (usually piezoelectric crystal based system);

- A control and image system that converts the measured data into an image.

An AFM can be operated in three modes: contact mode, non-contact mode and intermittent-contact mode. Fig. 1.3 shows the operative region of each mode, on a typical interatomic force-distance curve.
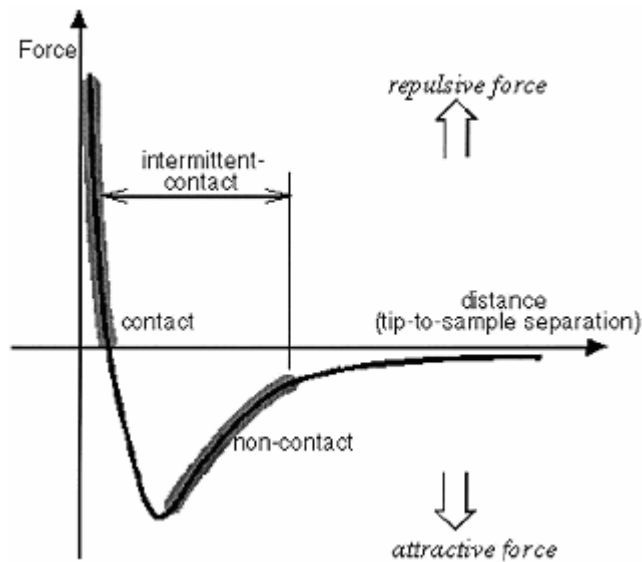
Figure 1.6: Interatomic force vs. distance curve

In contact mode, the tip is in contact with the sample, and repulsive forces between the tip and sample are measured. The total tip-surface force is the sum of both large range van der Waals (vdW) and short range chemical interactions. For distances below 2 A°, the chemical interaction is dominated by the Pauli repulsion and starts to balance the attractive vdW force. AFM images taken at small tip-surface distances, where the total tip-surface force is repulsive(the vdW interaction is smaller than the short range atomic repulsion), are said to be formed during contact mode.

In non-contact AFM mode, the tip is not in contact with the sample, and long-range interaction forces, e.g. vdW, electrostatic, and magnetic force can also be probed. Unlike contact mode, this method is sensitive to force gradient, rather than the interaction forces between tip and sample. The cantilever is driven to vibrate at its resonance frequency by means of a piezoelectric element, and changes in the resonant frequency as a result of tip-sample interaction are measured. The force gradient $F' = -\partial Fz = \partial z$ results in a modification of the effective spring constant of the cantilever.

$$k_{eff} = k - F' \tag{1.44}$$

where k is the spring constant of cantilever in the absence of tip-surface force interaction. An attractive tip-surface interaction with ($F' > 0$) will therefore soften the effective spring constant ($k_{eff} < k$), whereas a repulsive tip-surface force interaction ($F' < 0$) will strengthen the effective spring constant ($k_{eff} > k$). The change of the effective spring constant, in turn, produces a shift in the resonant frequency ω of the cantilever according to

$$\omega = \left(\frac{k_{eff}}{m}\right)^{1/2} = \left[\frac{(k-F')}{m}\right]^{1/2} = \left(\frac{k}{m}\right)^{1/2}\left(1-\frac{F'}{k}\right)^{1/2} = \omega_0\left(1-\frac{F'}{k}\right)^{1/2} \tag{1.45}$$

where m is an effective mass and ω_o is the resonance frequency of the cantilever in the absence of force gradient. If F' is small relative to k then Eqn. (1.45) can be approximated by

$$\omega \approx \omega_0\left(1-\frac{F'}{2k}\right) \tag{1.46}$$

and therefore

16

$$\frac{\Delta\omega}{\omega_0} \approx -\frac{F'}{2k} \qquad\qquad (1.47)$$

and attractive force with ($F' > 0$) will therefore lead to a decrease of the resonant frequency ($\omega < \omega_o$), whereas a repulsive force ($F' < 0$) will lead to an increase ($\omega > \omega_o$).

In intermittent-contact atomic force microscopy (IC-AFM) which is similar to nc-AFM, the cantilever tip is brought closer to the sample so that the bottom of it just barely hits, or "taps", the sample. As for nc-AFM, for IC-AFM, the cantilever's oscillation amplitude changes in response to tip-to-sample spacing. An image representing surface topography is obtained by monitoring these changes. Some samples are best handled by using IC-AFM instead of contact or non-contact AFM. IC-AFM is less likely to damage the sample than contact AFM because it eliminates lateral forces (e.g. friction) between the tip and the sample. In general, it has been found that IC-AFM is more effective than nc-AFM for imaging larger scan sizes that may include greater variation in sample topography. Different techniques have been employed for measurement the deflection of the cantilever and each technique has its own advantages and disadvantages.

1.5.1 Tunnelling Detection Method

The first AFM used an Scanning Tunneling Microscope (STM) tip to measure the cantilever detection by Binnig [17]. The STM tip is positioned behind the AFM lever, and used to measure the cantilever displacement. This method is very sensitive to contamination, roughness of the cantilever and to thermal drift, which make it rather unreliable.

1.5.2 Capacitance Detection Method

This method was first used by Neubauer [19]. The back of cantilever is used as one plate in a capacitor. As the lever bends, the change in its position results in a

change in the capacitance. The variation of the capacitance is measured and used to calculate the deflection of the lever. The sensitivity is dependent on the smoothness and distance between the plates. The sensitivity of this technique to uniform smoothness of surfaces and distance between the plates. The sensitivity of this technique is of the order of 1 x 10^{-2} A°/ $Hz^{1/2}$.

1.5.3 Optical Beam Deflection Method

This technique is first employed by Meyer and Amer [20,21].A laser beam is reflected from the back of the cantilever onto a two-cell photodiode. Force on the tip causes the cantilever to bend, and the position of the reflected laser spot moves, causing a change in the relative intensity of the photodiode signals, this technique has been later extended, using a four-cell photodiode to measure the twisting of the cantilever and hence the lateral force on the tip. This technique has a sensitivity of better than 5 x 10^{-3}A°/ $Hz^{1/2}$.
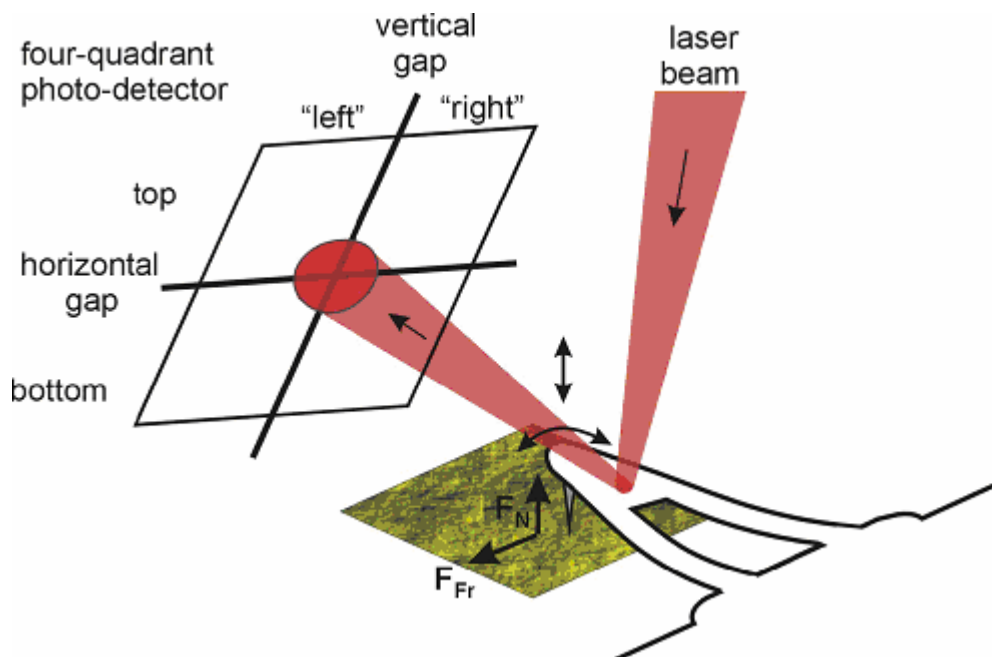
Figure 1.7: Diagram for OBD method in AFM

1.5.4 Optical Fiber Based Interferometry (OFBI) Method

Deflection measurement with optical interferometry [22] is the most sensitive and appropriate method for UHV condition. In this method, multiple reflections are obtained which form a Fabry- P`erot interferometer cavity between the end of the fiber and the back of the cantilever. This causes radical enhancement in the sensitivity.
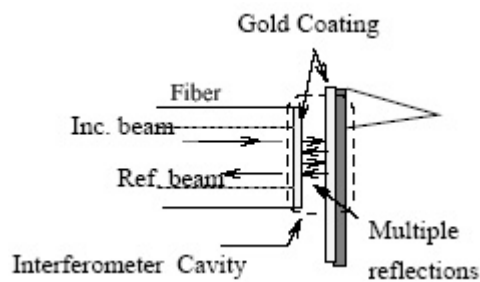
Figure 1.8: Diagram for OFBI in AFM

1.5.5 Quartz Tuning Fork Based Method

The tuning forks have been successfully employed for Atomic Force Microscopy [23]. The advantages of these piezoelectric sensors are the availability, the low cost, and the high quality factors. One arm of the tuning fork used as cantilever mount which is oscillated at the resonance frequency and the other arm gives the output signal by means of induced voltage by deflection. Fig. 1.9 shows the close-up picture of a cantilever mounted tuning fork and Fig. 1.10 shows how it is drived electronically at operation.
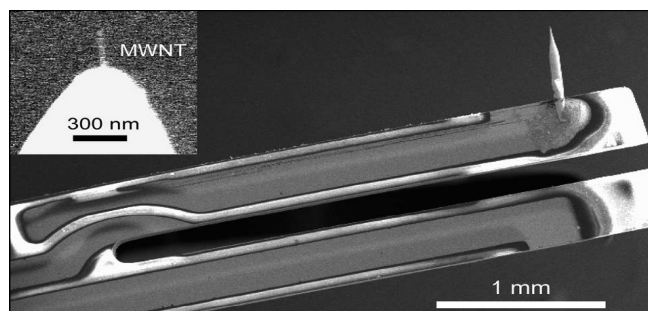
Figure1.9: A close-up picture of a cantilever mounted tuning fork

19
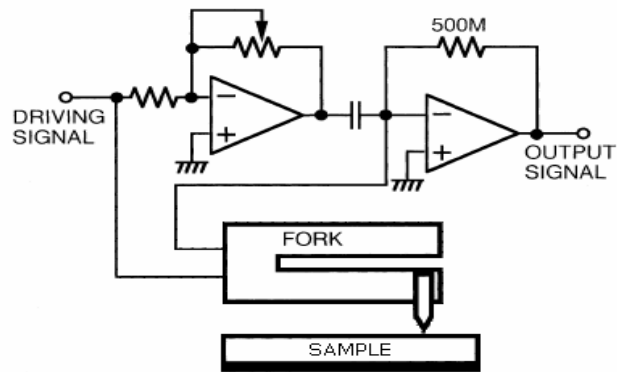
Figure 1.10: Schematic diagram of driver circuit for tuning fork

In this work, a quartz tuning fork sensor based AFM (QTF-AFM) has been used for getting surface images. It is simple to operate and fast to reoperate. It can reach a resolution up to some nanometers in an ideal situation.

Figure 1.11: The picture of QTF AFM [24]

CHAPTER 2

Sample Preparation

In this chapter, the methods and the tools used for sample growth have been described. We have grown thin films by using a thermal evaporation system in a Hall bar structure. The contacts from samples have been taken by copper wires fixed on Gold layers deposited on the terminals. They have been characterized electrically in a Hall effect and magnet system.

2.1 Thermal Evaporation System

Thermal evaporation technique has been used to deposite the polycrystalline Bismuth thin films. Because this method is fast and cheap although the other methods produce higher quality films [2]. However we think that the overall study should be suitable for industrial purposes because industry seeks for development methods which are feasible in price and in time.

To obtain a thin film without any contamination which may have negative effect in the electrical and the structural properties of the film, the evaporation process should be carried out in vacuum condition. The base pressure of the thermal evaporation system was better than 4.0×10^{-6} mbar. The evaporation system consists of a vacuum chamber, rotary pump and a diffusion pump and the corresponding valves between each part and pressure detectors. Schematic view of the system is shown in Fig. 2.1.
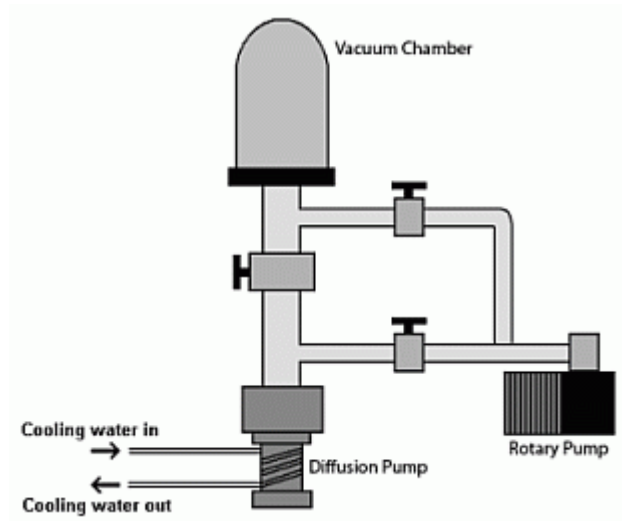
Figure 2.1: Schematic view of thermal evaporation system

To measure the pressure on the chamber, a pirani and an ion gauges are employed. A pirani gauge can measure the pressure down to 3.5×10^{-3} mbar. Beyond this pressure an ion gauge must be used to monitor the pressure which can measure down to Ultra High Vacuum that is better than 1.0×10^{-10} mbar.

A rotary pump was used for rough pumping of the system and can achieve a pressure about 5.0×10^{-3} mbar. It simply sucks the air out. After rough pumping a diffusion pump was operated and can achieve a better pressure than 4.0×10^{-6} mbar. The diffusion pump captures the ions in the medium. To cool the diffusion pump, a copper pipe was wounded around the pump body and tap water was let through the pipe (Fig. 2.1).

The vacuum chamber has a flat base and a glass bell jar upon that flat base. The bell jar can easily be removed from the base after breaking vacuum. When placing it, a vacuum greased special plastic gasket is put between the ball jar and the base.

In the vacuum chamber, bismuth was placed on a tungsten boat. The tungsten boat was attached to two copper terminals from each end in which current was applied. Between boat and substrate holder, a shutter was used to control the flux.

22

It took about a few minutes to remove the oxides on boiling bismuth. The shutter can easily be operated by using the outside extension of the rod that holds the shutter. The picture of the thermal evaporation system can be seen in Fig. 2.2.

Figure 2.2: The picture of the thermal evaporation system

2.2 Substrate Preparation

Glass substrates have been used for bismuth thin film growth. For different applications, substrates with different sizes have been used. For Hall effect and XRD studies in 25mm x 25mm substrates and for AFM studies in 5mm x 5mm substrates have been used. The procedure for substrate cleaning process before growing is given below:

- Substrates are placed in hot water with a gentle soap in an ultrasonic bath.
- A pure water is used to remove the soap several times in an ultrasonic bath.
- Pure acetone is used in an ultrasonic bath.
- Substrates are placed in pure propanol and left for some minutes.
- After removal of each substrate, flow of propanol on surface is checked and pressurized nitrogen is used for quick removal of the propanol on the surface.

2.3 Bismuth Growth

After reaching a successful pressure ($<4 \times 10^{-6}$ mbar), bismuth thin film was grown on substrates which had already been placed in corresponding holders. The samples for XRD and AFM study did not have a special structure on the film. However, for Hall effect studies a Hall bar mask was used in growth which is shown in Fig. 2.3.

Figure 2.3: Hall bar shadow mask

Two end terminals of bismuth film in Hall bar structure are used typically to apply current and one couple of transverse terminals are used to monitor the voltage on sides of the film when it is subjected to a magnetic field.

2.4 Electrical Contacts and Wiring

Gold and bismuth have shown ohmic contact. For the samples which would be used in Hall effect studies, in each terminal point, 100 nm gold layer has been deposited after deposition of 10 nm titanium buffer layer which sticks to bismuth better than gold and makes the gold contacts physically more stable. Finally, electrically insulated copper wires with a diameter of 300μ were cured to gold surfaces with silver paint. Figure 2.4 shows the contact structure of Hall effect samples.
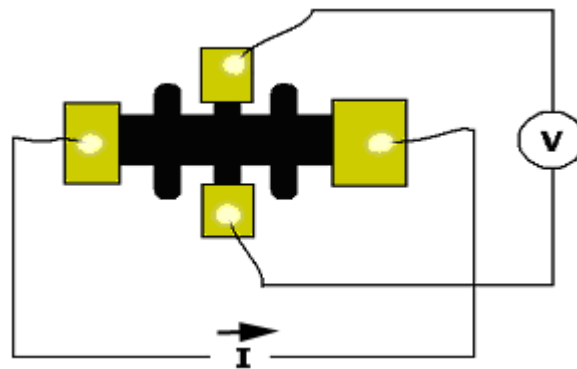
Figure 2.4: Hall bar sample

2.5 Annealing System

Bismuth tends to oxidize easily. Therefore, annealing should take place under an inert gas. The annealing system has an aluminum hot plate with an embedded resistance heater in which the sample is placed. The flow of nitrogen in was has been kept continuous because of continuous escape of the gas during annealing. The temperature on the plate has been monitored by a thermocouple attached to the surface of the hot plate.

Figure 2.5: Schematic representation of the annealing system

We have used the same setup for oxidization by pure oxygen gas flow. The only difference on the process is that oxygen is flammable and the process should be performed very carefully.

2.6 Cryostat and Hall Effect System
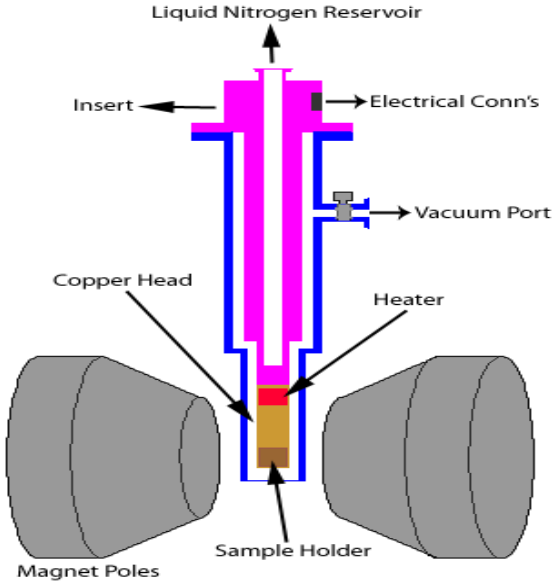
Figure 2.6: Schematic representation of the cryostat and magnet system [25]

The hall bar sample has been placed in and electrically connected into sample holder part in the Insert in Fig. 2.6. In the 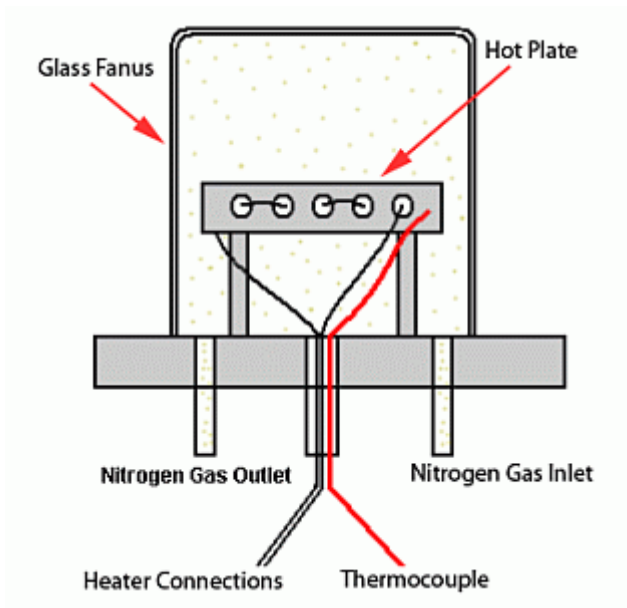copper head, a heater and a thermocouple has been used to control the temperature by a temperature controller (LakeShore 331) at the sample. After mounting the sample, inside of vacuum dewar was evacuated to ~4.5 10^{-3} Torr by a rotary pump. After checking the ohmicity of the contacts, liquid Nitrogen was filled into liquid nitrogen reservoir. We kept evacuating till making sure that the liquid Nitrogen reservoir was empty. We have performed our measurements from 80K to 350K in a constant magnetic field. The magnet system that we have used in our experiments can provide ~ 1.0T magnetic field.

CHAPTER 3

Results and Discussions

In this chapter, the electrical and structural results for two different thicknesses (30nm and 90nm) of Bismuth thin films have been analyzed. Each sample with different thickness has its own Hall bar sample. The samples for both thicknesses have been subjected to the same procedure. Their electrical and structural data have been presented for as-grown sample, annealed sample at 100°C and 150°C for 45 minutes and oxidized sample at 150°C for 45 minutes. Each thickness of the films has its own results and discussions section including its electrical and structural properties. The thin film samples were studied in a temperature range of 80 - 350K Their electrical properties have been analyzed for as-grown, annealed and oxidized forms at the same time. For crystallinity studies, their X-Ray Diffraction (XRD) results have been discussed. XRD patterns have also been used to obtain the orientation directions of the films. By using AFM results, it is possible to see the effects of the film thickness, annealing and oxidization on the film surface. We have also used a high magnification optical microscope (x100) to compare the results with the AFM results.

3.1 30 nm Bismuth Thin Film

3.1.1 Electrical Properties

The electrical properties of thin films can be characterized by conductivity and Hall effect measurements. Also, the activation energies from those properties can be calculated by using corresponding temperature dependent behaviors of the conductivity, mobility and carrier concentrations. This section includes the discussion of the electrical properties of 30nm thin film.

3.1.1.1 Conductivity Measurements

Conductivity measurements have been carried out as a function of temperature in the range of 80 - 350 K and annealing at 100 and 150°C for all samples. As seen from Fig. 3.1, the conductivity of the samples is increasing exponentially with increasing ambient temperature. However, the variation of conductivity with temperature is quite small. This means that the samples have almost metallic behavior, as compared to the semiconductors. Furthermore, the same samples after measurement have been annealed at 100 and 150°C under nitrogen atmosphere. The annealing of the samples at constant ambient temperature does not yield any pronounced effects on the conductivity of the samples, they show the same values with slight changes.

The variation of the conductivity with the temperature shows three temperature regions with different slope values. In the high temperature regions, conductivity shows sharp increases and in the low temperature regions, the variation of conductivity is almost constant, and also there is an other mid-temperature regions which are transition regions between high and low temperature regions. Therefore referring to Eqn. 1.36, it is possible to find activation energies of conductivity (E_a) for those regions (see Table 3.1). To see the effect of oxygen on Bi thin films, some of the samples have been annealed under the oxygen atmosphere for 45 minutes. We observe that after the oxidizing the samples, conductivity values are increasing much more than annealing under the inert gas. This implies the changes of structure of the samples with insertion of oxygen atom to the Bi structure.
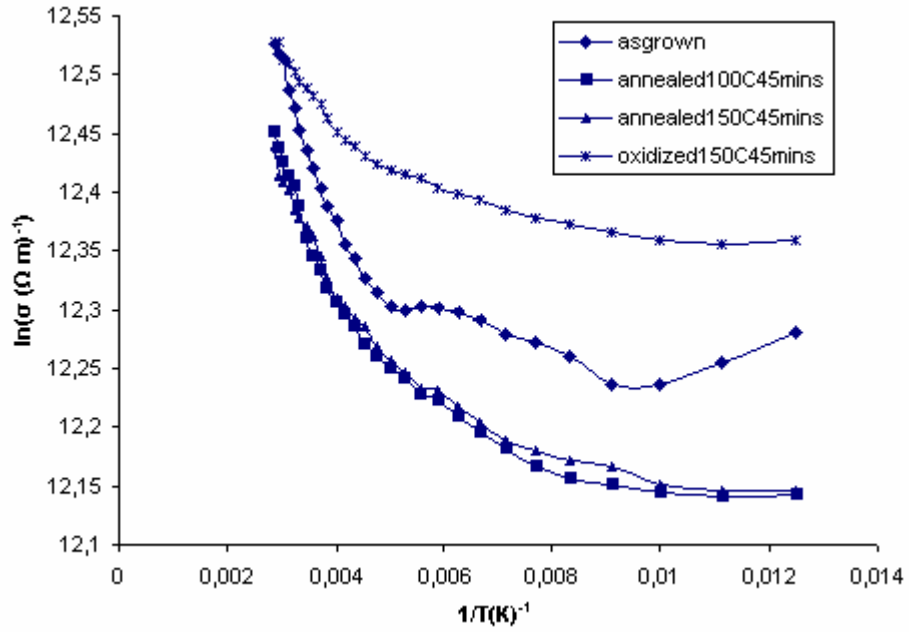
Figure 3.1: Semilogarithmic plot of conductivity versus inverse temperature for 30nm thin film

Table 3.1: Activation energies of 30nm Bi thin film obtained from conductivity-temperature dependence

sample	High temperature region (350-260)K	Mid temperature region (260-160)K	Low temperature region (160-80)K
As-grown	10.6 meV	1.4 meV	0.2 meV
Annealed at 100°C for 45mins	11.9 meV	2.9 meV	0.5 meV
Annealed at 150°C For 45mins	8.2 meV	2.6 meV	0.9 meV
Oxidized at 100°C For 45mins	5.7 meV	1.4 meV	0.6 meV

The activation energy values calculated from conductivity given in Table 3.1 are very small. It shows that the structure has metallic properties where there is no distinction between valence and conduction bands.

3.1.1.2 Mobility

Mobility is a measure of the motion of an electron in the applied electric field. When an electron moves in a field, its mobility is a subject for some scattering mechanisms which act on the electron as a function of temperature. Those mechanisms are lattice scatterings and impurity scatterings. It is possible to get an idea about scattering mechanisms on the sample by mobility versus temperature plot (Fig. 3.2). To investigate the scattering mechanisms quantitatively, logarithmic plots of mobility-temperature behaviors have been obtained (Fig. 3.4). We theoretically expect a slope values of +3/2 or -3/2 to decide which mechanism is dominant. However the plot does not give us expected slope values that are given in Table 3.2. The slope values show that the scattering mechanisms are combination of impurity and lattice scatterings. We can conclude that phonon scattering is dominant for negative slope values and when it is positive, the impurity scattering is dominant. At high temperature regions (>250K) the lattice (or phonon) scattering seems to dominant. Since, in that region, $Ln(\mu)$-$Ln(T)$ plot gives negative slopes with small values.
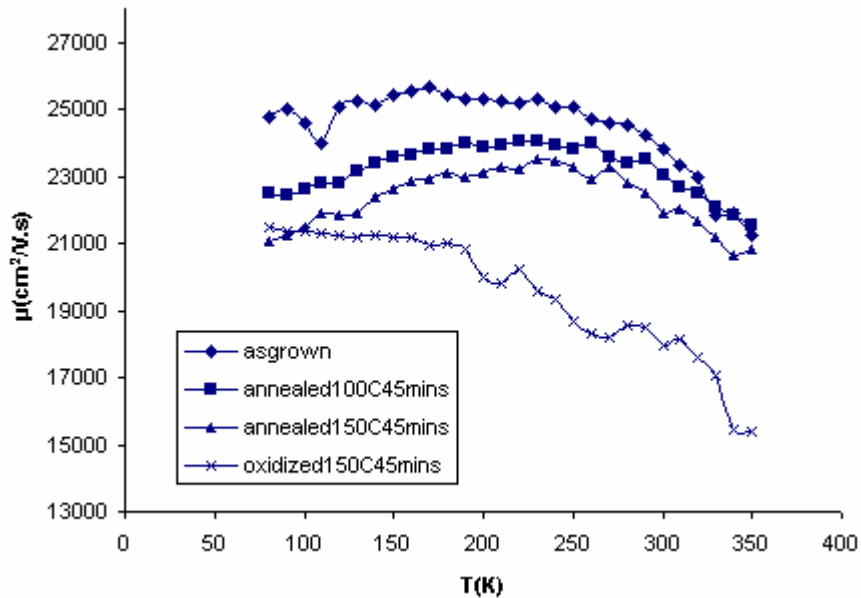

Figure 3.2: Mobility versus temperature plot for 30nm Bi thin film

It is also possible to calculate activation energies from semilogarithmic plot of mobility versus inverse temperature (Fig. 3.3), because there is an exponential dependence between mobility and temperature govern from conductivity and carrier density. However, for these films, the variation of mobility with inverse temperature is quite small because of the metallic behavior. Therefore 30nm thin film does not enable us to calculate the grain boundary potential because it shows a linear behavior by increasing temperature.
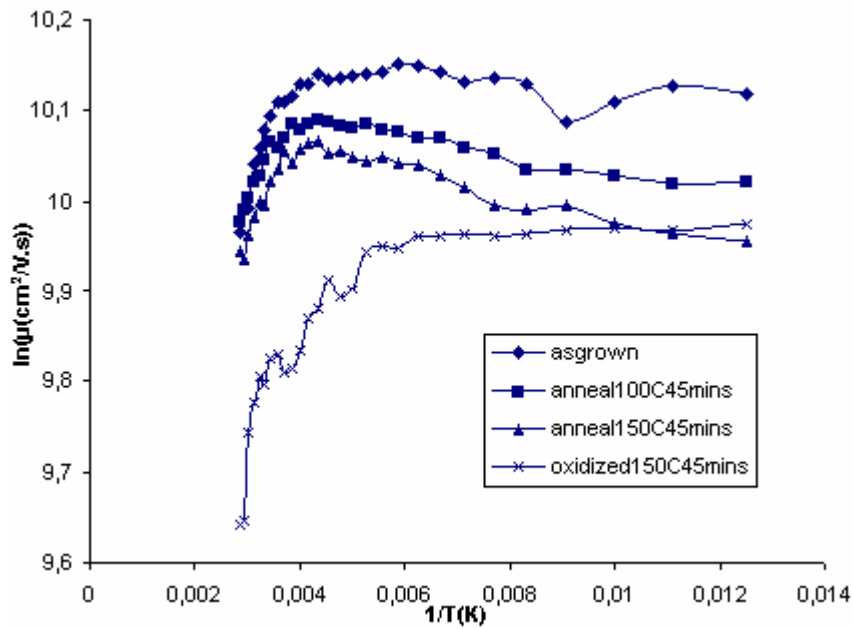

Figure 3.3: Semilogarithmic plot of mobility versus inverse temperature for 30nm Bi thin film
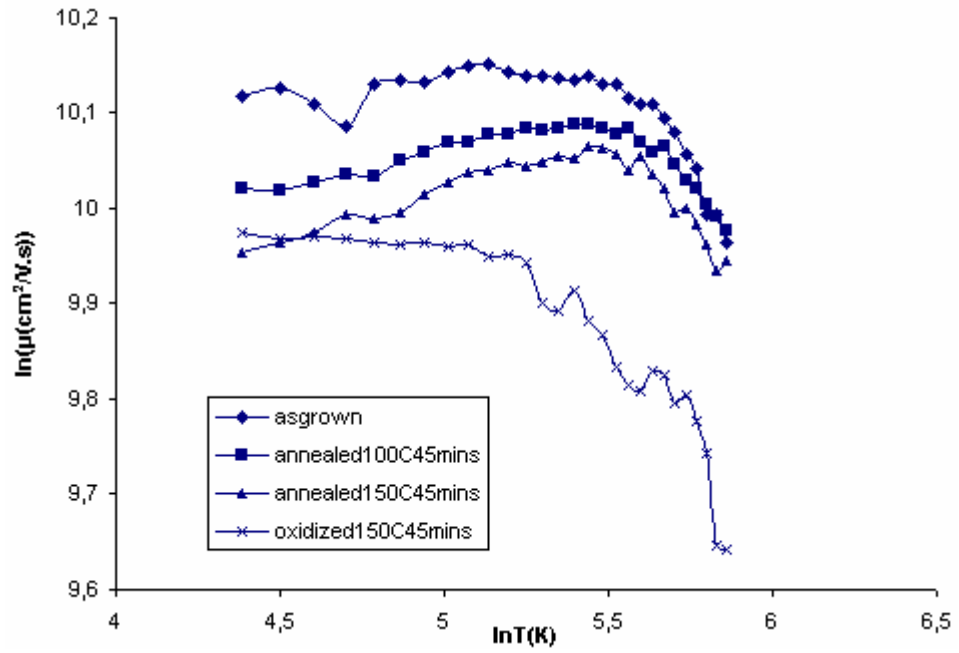
Figure 3.4: Logarithmic plots of mobility-temperature behaviors for 30nm Bi thin film

Table 3.2: Slope values of logarithmic plots of mobility-temperature behaviors for 30nm Bi thin film

sample	Low Temperature region (80-260)K	High temperature region (260-350)K
As-grown	0.065	-0.702
Annealed at 100°C for 45mins	0.095	-0.453
Annealed at 150°C for 45mins	0.113	-0.489
Oxidized at 100°C for 45mins	-0.017	-0.408

3.1.1.3 Carrier Concentration

Oxidization is a process like doping increasing the carrier concentration (Fig.3.5). We expect to see some positive changes on crystal structure so that it shows more semiconductor properties. The activation energies of the sample can also be calculated from semilogarithmic plot of carrier concentration versus inverse temperature (Fig. 3.6) which are given in Table 3.3. We conclude that the oxidization of the sample has increased the activation energies of the sample at all temperature regions.
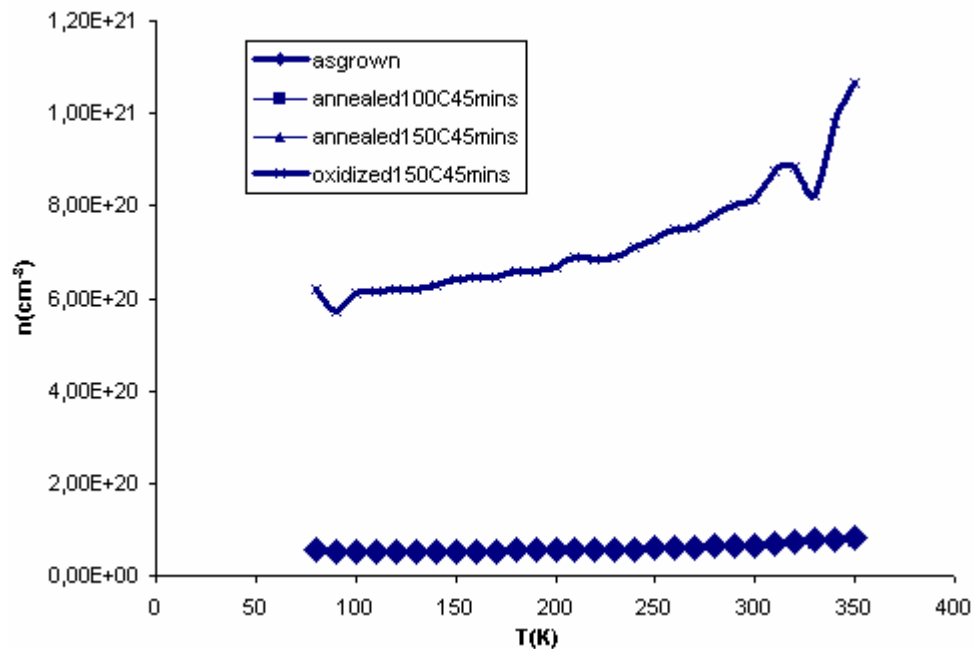

Figure 3.5: Carrier concentration versus temperature plot for 30nm Bi thin film
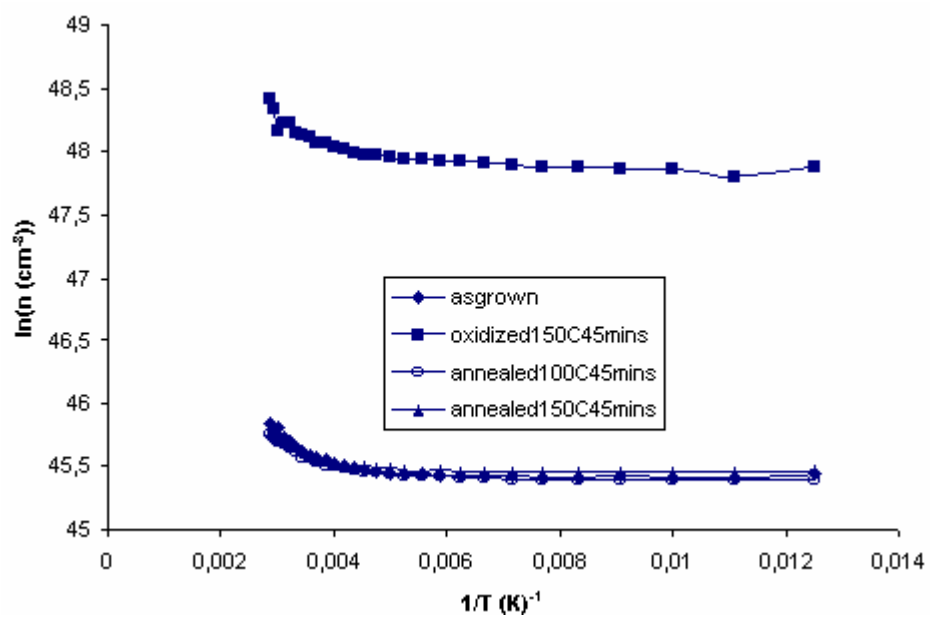
Figure 3.6: Semilogarithmic plot of carrier concentration versus inverse temperature for 30nm Bi thin film

Table 3.3: Activation energies of 30nm Bi thin film obtained from concentration-temperature dependence

sample	Low temperature region (80-260)K	High temperature region (350-260)K
As-grown	2.9 meV	28.2 meV
Annealed at 100°C for 45 mins	2.8 meV	28.2 meV
Annealed at 150°C for 45 mins	2.9 meV	28.1 meV
Oxidized at 100°C for 45 mins	3.7 meV	35.7 meV

3.1.2 XRD Results

The structural analysis of the samples has been carried out by X-ray diffraction technique. The X-ray diffraction pattern taken over as-grown samples shows that the Bi films have polycrystalline structure as seen from Fig. 3.7. The reflection along (4 4 2) direction shows that the preferred orientation direction for as-grown and annealed samples when we have compared X-ray patterns with ICDD (Crystal Database). It has been observed that Bi_2O_3 crystal data fits the diffraction patterns and has 2 phases of Bi_2O_3: monoclinic and tetragonal. Diffraction peaks 1 and 3 referred to Bi_2O_3 tetragonal phase while diffraction peaks 2 and 4 referred to Bi_2O_3 monoclinic phase. We can mark some slight changes on the diffraction peaks after annealing and oxidization processes. As seen in Fig. 3.7, annealing at 100°C does not affect the crystallinity as annealing at 150°C does. Therefore we can say that 150°C is a more suitable annealing temperature for Bi samples.
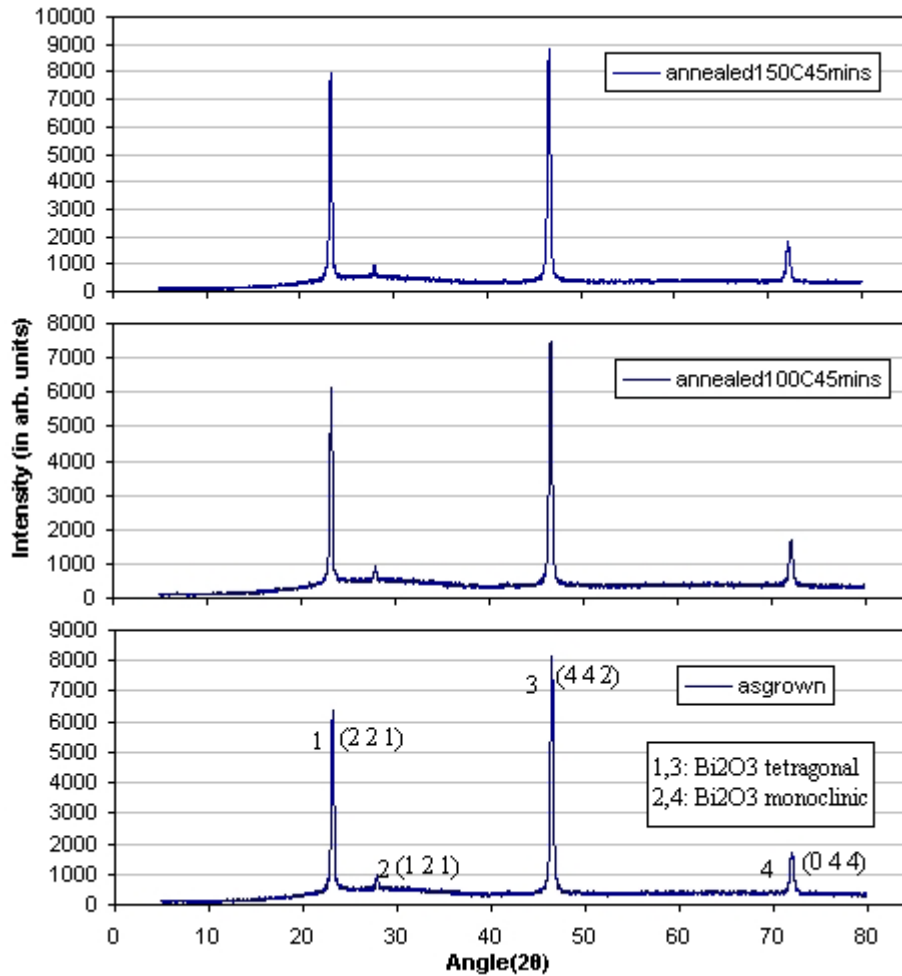
Figure 3.7: XRD pattern of 30nm Bi thin film at different annealing temperatures

3.1.3 AFM Results

The study of surface morphology of materials is a general topic of interest from Physics to Biology. Scanning Probe Microscopy (SPM) provides different application methods for different applications. AFM, as a powerful tool of SPM, enables us to scan surfaces without any electrical requirement. Non-contact AFM mode (nc-AFM) is a successful method because of being non-invasive for senssitive surface studies as the contact mode is mostly used for power dissipation and friction studies. So a QTF-AFM has been employed for surface studies of Bismuth thin film.

Thin film growth by thermal evaporation is a process starting with cluster formation on the substrate surface and continuing with combination of those

37

clusters. Those clusters have their own crystal structure forming a grain. In as-grown sample (see Fig. 3.8), AFM image shows that the grain sizes are small and the corrugation on the surface is high. Annealing at 100°C for 45 minutes made the surface a bit smoother (see Fig. 3.9) and grain sizes greater but not as much as annealing at 150°C did. Annealing the samples at 150°C for 45 minutes produced a smoother surface with higher grain sizes (see Fig. 3.10) which showed us that this annealing conditions were capable to migrate the atoms between grains. The histogram curves shows a sharper peak as the surface is getting smoother. Histogram data shows the data distribuiton all over the image. Annealing the samples at 150°C affected the structure more than annealing the samples at 100°C did. Those results are a good agreement with our XRD results (Fig. 3.7). Because in XRD pattern, we saw that the effect of second annealing was more visible in crystal structure resulting in the growth in grains. In each annealing temperature, it is obvious that the atoms have the chance of migrating between grains to minimize the surface energy. It is a process that will take long time in room temperature. Increasing temperature gives energy to the grains and makes to process faster; however, a temperature more than half of melting point of Bismuth (271°C) is more successful to make the process faster.
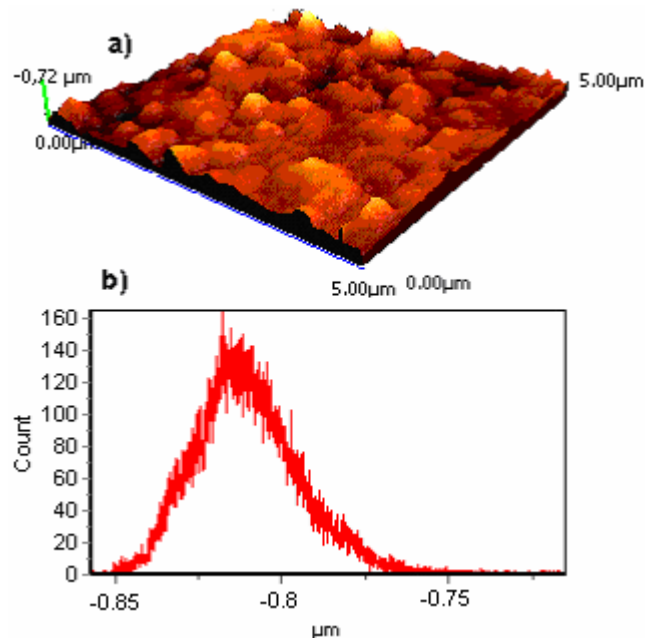

Figure 3.8: a) 3D AFM image (5µm x 5µm, 256 x 256 pixels), b) Histogram data, of as-grown 30nm Bi thin film
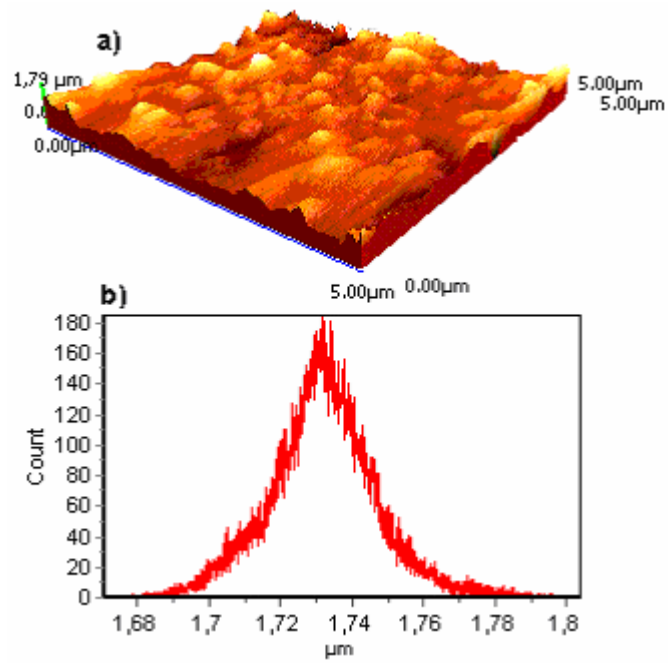
Figure 3.9: a) 3D AFM image (5μm x 5μm, 256 x 256 pixels), b) Data histogram, of annealed at 100$^{\text{o}}$C for 45 minutes 30nm Bi thin film
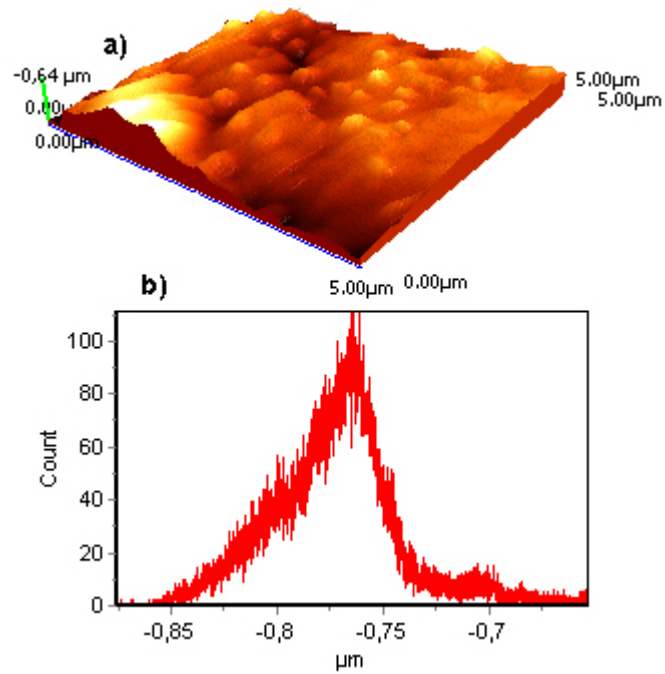
Figure 3.10: a) 3D AFM image (5μm x 5μm, 256 x 256 pixels), b) Data histogram, of annealed at 150$^{\text{o}}$C for 45 minutes 30nm Bi thin film

The effect of oxidization on the sample is shown in Fig. 3.11. After oxidizing the sample, we see some new but small features on the surface. So, some oxide islands have started to form on the surface. But they are relatively small because of the annealing temperature was not high enough.

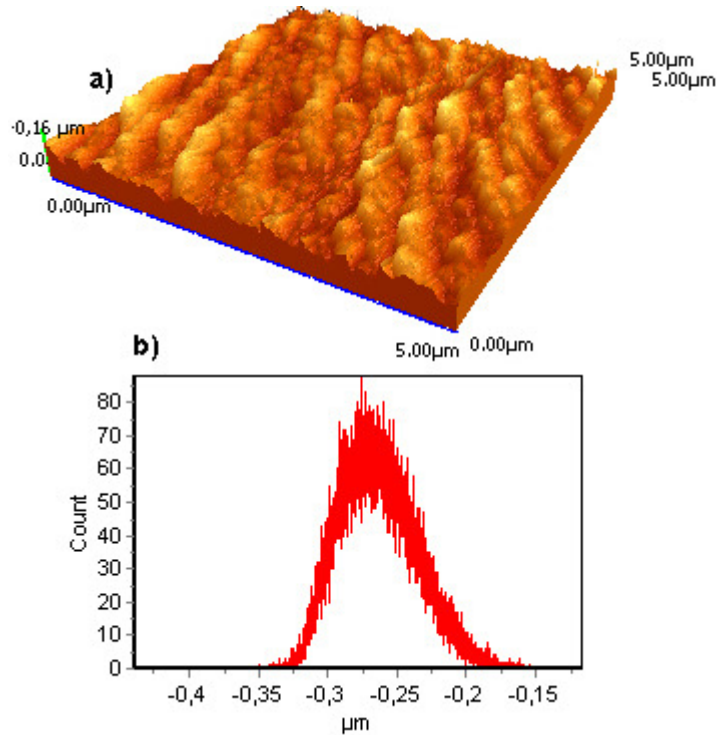

Figure 3.11: a) 3D AFM image (5µm x 5µm, 256 x 256 pixels), b) Data histogram, of oxidized at 150°C for 45 minutes 30nm Bi thin film

3.1.4 Optical Microscope Results

We also used an optical microscope to enlarge our view on the surface. The typical magnification we used was x100. We see, in each step of annealing process, the grains grow more (see Fig.s 3.12, 3.13, 3.14). However, as seen from optical images, the behavior of growth competes with X-ray and AFM results. Annealing the samples at 150°C has pronounce effect.
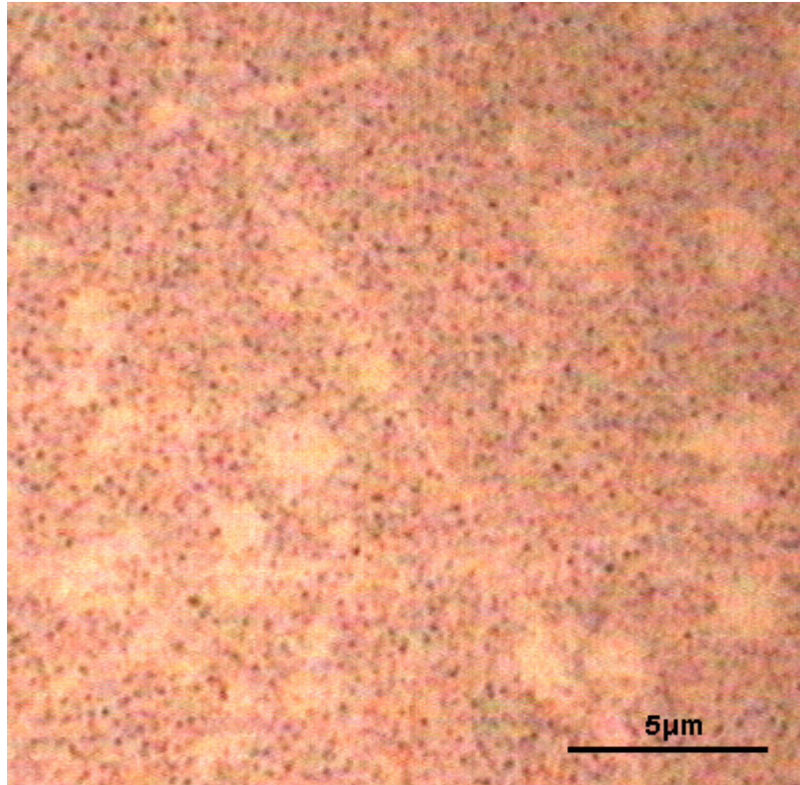
Figure 3.12: 20μmx20μm optical image of as-grown 30nm Bi thin film
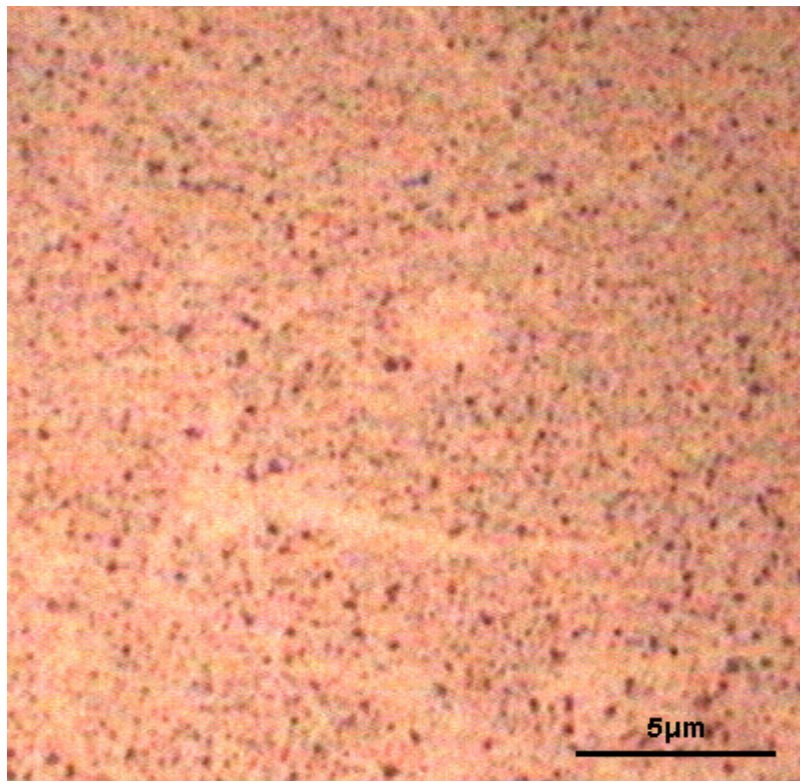
Figure 3.13: 20μmx20μm optical image of 30nm Bi thin film annealed at 100°C for 45minutes
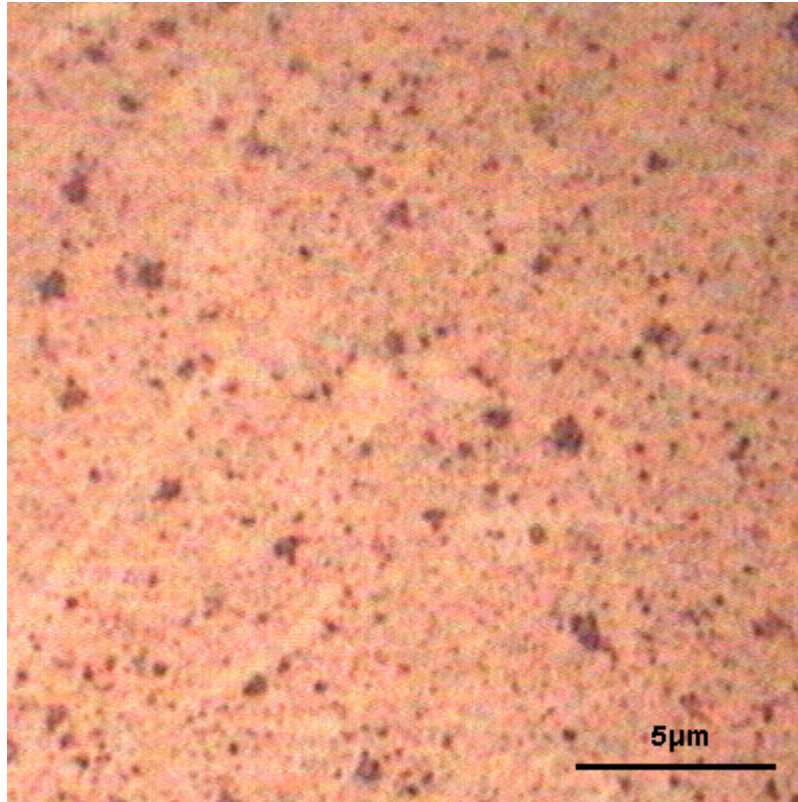
Figure 3.14: 20μmx20μm optical image of 30nm Bi thin film annealed at 150°C for 45minutes

3.2 90 nm Bismuth Thin Film

3.2.1 Electrical Characterization

We used the same procedure as we applied in section 3.1 for 90nm thin film. We characterized 90nm Bismuth thin film by measuring temperature dependent conductivity and mobility. This section analyses and discusses the electrical properties of 90nm thin film in the form of subsections for different electrical parameters.

3.2.1.1 Conductivity Measurements

In the conductivity measurements of 90nm thin film, the variation of conductivity

as a function of temperature in the semilogarithmic plot of conductivity versus inverse temperature is small so that the structure has metallic properties more than 30nm thin film as seen from Fig.3.15. However, only oxidized sample shows an increase on conductivity which is more than oxidized 30nm thin film. So the oxidization shows a larger effect on the thicker film.
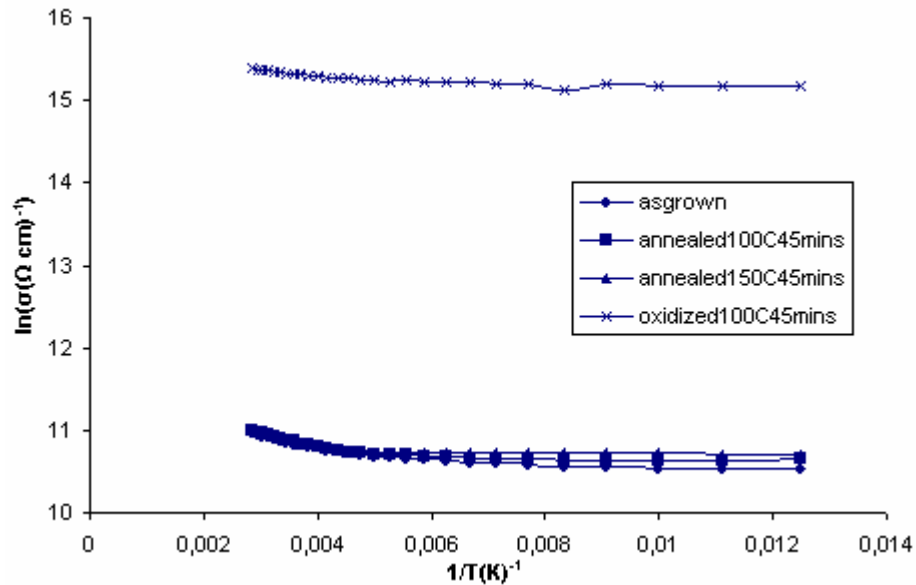

Figure 3.15: Semilogarithmic plot of conductivity versus inverse temperature for 90nm Bi thin film

The activation energies (E_a) obtained from slopes of semilogarithmic plot of conductivity versus inverse temperature (Fig. 3.15) were calculated and given in Table 3.4. The oxidization decreases the activation energy values at all temperature regions in between 80 to 350K.

Table 3.4: Activation energies of 90nm Bi thin film obtained from conductivity-temperature dependence

sample	High temperature region (350-260)K	Mid temperature region (260-160)K	Low temperature region (160-80)K
As-grown	13,5 meV	1,6 meV	0,2 meV
Annealed at 100°C for 45mins	12,4 meV	3,1 meV	0,9 meV
Annealed at 150°C for 45mins	15,1 meV	1,4 meV	0,4 meV
Oxidized at 100°C for 45mins	6,8 meV	2,0 meV	0,4 meV

For 90nm thin film, we see that the structure has metallic properties because of low activation energy values as seen from Table 3.4 as 30nm thin film has.

3.2.1.2 Mobility

We expect to get an idea about scattering mechanisms from mobility versus temperature plot. However the behavior that we have found does not give any idea about scatterring mechanisms except the oxidized sample in Fig. 3.16. The oxidized sample shows that some lattice effects on the scattering mechanisms started to be dominant at higher temperatures.
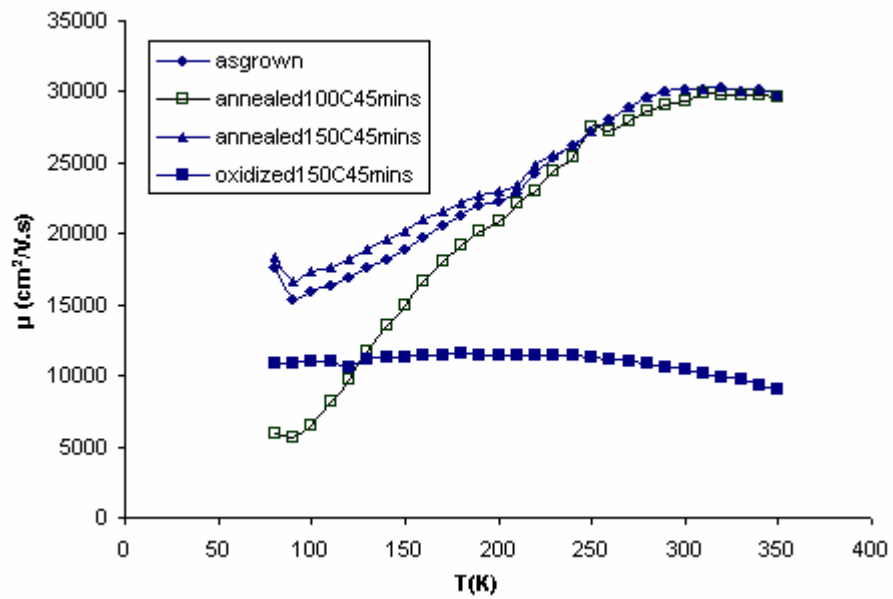
Figure 3.16: Mobility versus temperature plot for 90nm Bi thin film

The behavior of semilogarithmic plot of mobility versus inverse temperature (Fig. 3.17) does not make us enable to calculate activation energies. It shows the structure is a degenerate behavior.
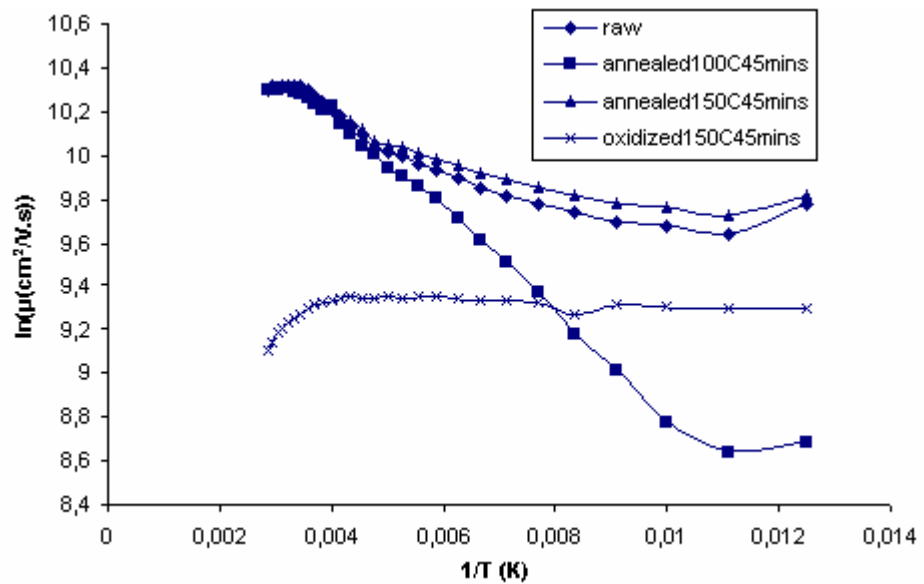

Figure 3.17: Semilogarithmic plot of mobility versus inverse temperature for 90nm Bi thin film
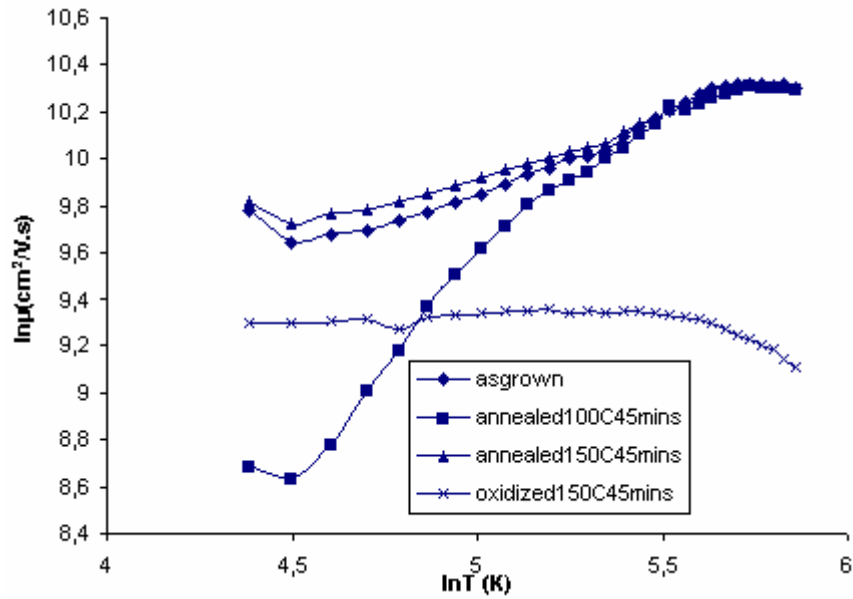
Figure 3.18: Logarithmic plots of mobility-temperature behaviors for 90nm Bi thin film

For detection of scattering mechanisms quantitatively, we could not be able to obtain any scattering mechanisms because of almost-linear mobility-temperature dependence for 90nm thin film (see Table 3.5).

Table 3.5: Slope values of logarithmic plots of mobility-temperature behaviors for 90nm thin film

sample	Low Temperature region (80-260)K	High temperature region (260-350)K
As-grown	0.520	Almost linear
Annealed at 100°C for 45mins	1.843	Almost linear
Annealed at 150°C for 45mins	0.424	Almost linear
Oxidized at 100°C for 45mins	Almost linear	-0.608

3.2.1.3 Carrier Concentration

The carrier concentrations of as-grown and annealled samples follows almost a similar variation and keeps the same as we expect. However, after oxidization, the increase in the carrier concentration is more than that of oxidized 30nm thin film (Fig. 3.19). We have also observed the increase on the conductivity of the thicker sample was higher. So we can say that thicker sample is more suitable to oxidization. The slope values in semilogarithmic plot of carrier concentration versus inverse temperature do not give us satisfactory results for activation energies (Fig. 3.20). Only the sample oxidized under 150°C for 45 minutes gives a behavior to calculate activation energies and for high temperature region of 300-350K. It is 20.6 meV.

Figure 3.19: Carrier concentration versus temperature plot for 90nm Bi thin film

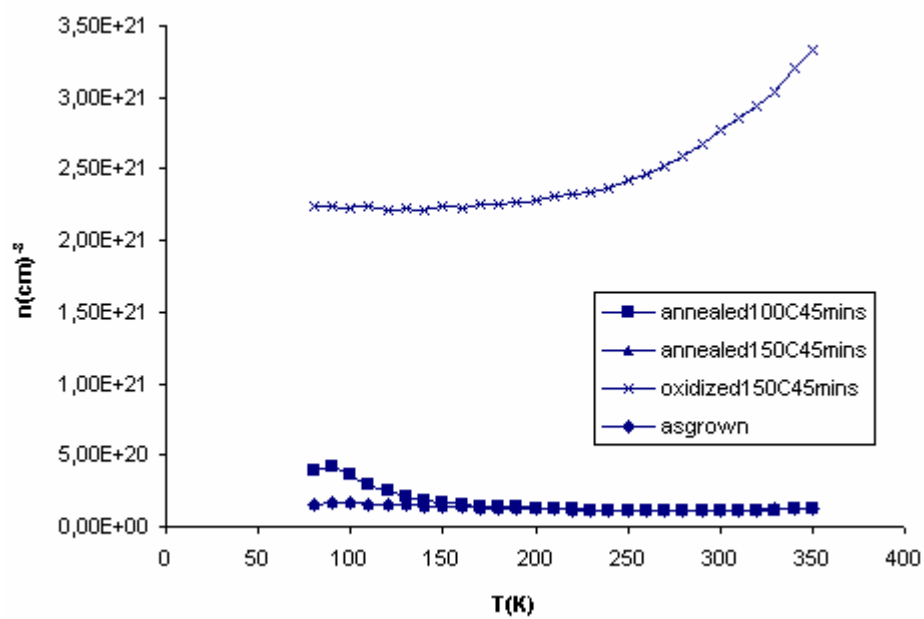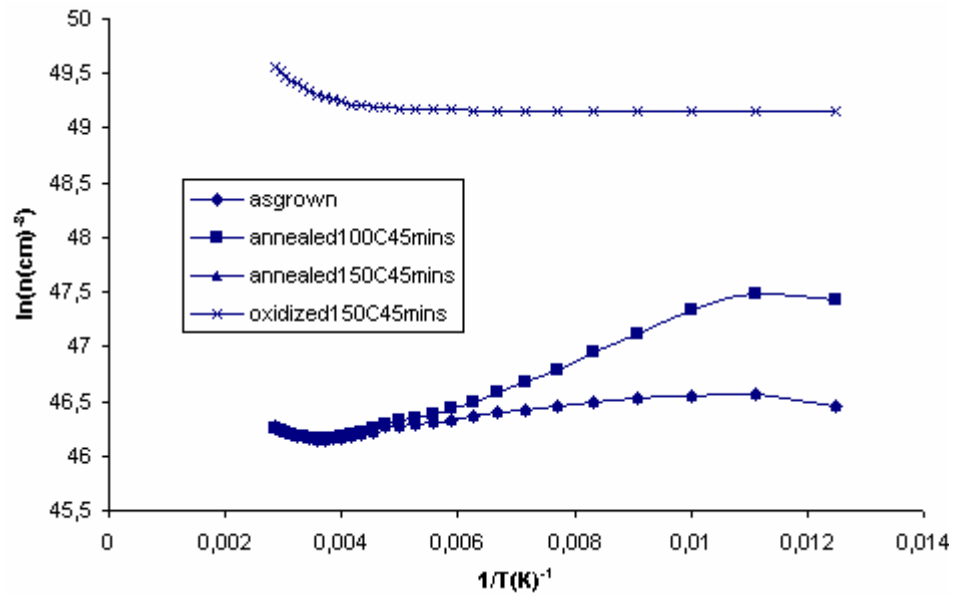Figure 3.20: Semilogarithmic plot of carrier concentration versus inverse temperature for 90nm Bi thin film

3.2.2 XRD Results

In the XRD pattern, we observed again that the samples had Bi_2O_3 (tetragonal) and Bi_2O_3 (monoclinic) from ICDD database [26]. And it seems that the direction of orientation in the structure is (4 4 2) which corresponds to the peak 3 that is the highest peak in the XRD diffractograms (Fig. 3.21).

After annealing 90nm thin film at $100^{o}C$ for 45 minutes and $150^{o}C$ for 45 minutes, we could not observe any change at X-ray spectrum as 30nm thin film. Then we annealed the sample at $150^{o}C$ for 60 minutes so that we were able to see a change on the film resulting with an increase on the spectrum which showed us a growth on the grains. It means that thicker films may require longer annealing times. After oxidizing the film, intensity slightly decreases showing the effect of the oxide on the surface as we expect.
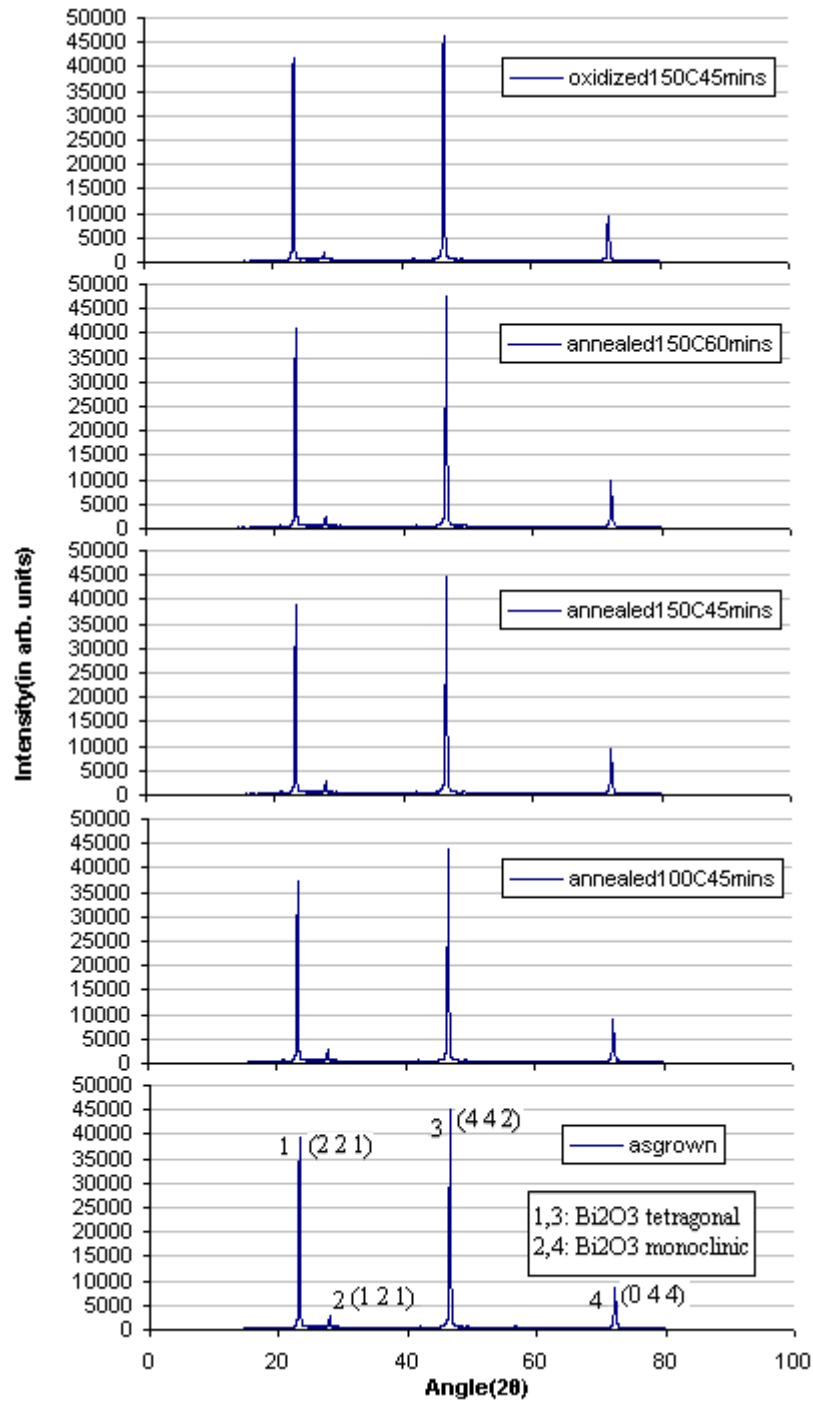
48

Figure 3.21: XRD pattern of 90nm Bi thin film at different annealing temperatures

3.2.3 AFM Results

In AFM studies of 90nm thin film, we have applied the same experimental conditions to make the AFM results respectively more reliable. We again used a QTF-AFM and AFM images have been taken 5µm x 5µm size in 256 x 256 pixels. We see, in Fig. 3.22, that the surface of the as-grown sample is smoother than that of 30nm showing us the surface becomes smoother as the thickness increases. Annealing the sample has shown some pronounce effects on the thicker film; however, the sample annealed under 150°C for 45 minutes has a considerable change on the surface as seen from Fig. 3.24. We observe that its surface area tries to minimize and has a smoother surface but not a plane. However, it may be a configuration for the surface which has a smaller surface energy if we think about the roughness on the substrate. We conclude that annealing at 150°C is more effective on the material than annealing at 100°C.
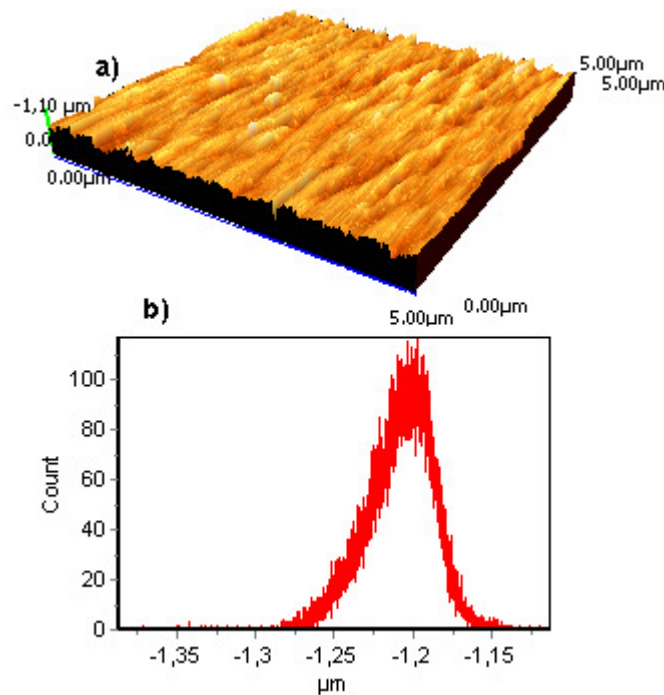

Figure 3.22: a) 3D AFM image (5µm x 5µm, 256 x 256 pixels), b) Data histogram, of as-grown 90nm Bi thin film

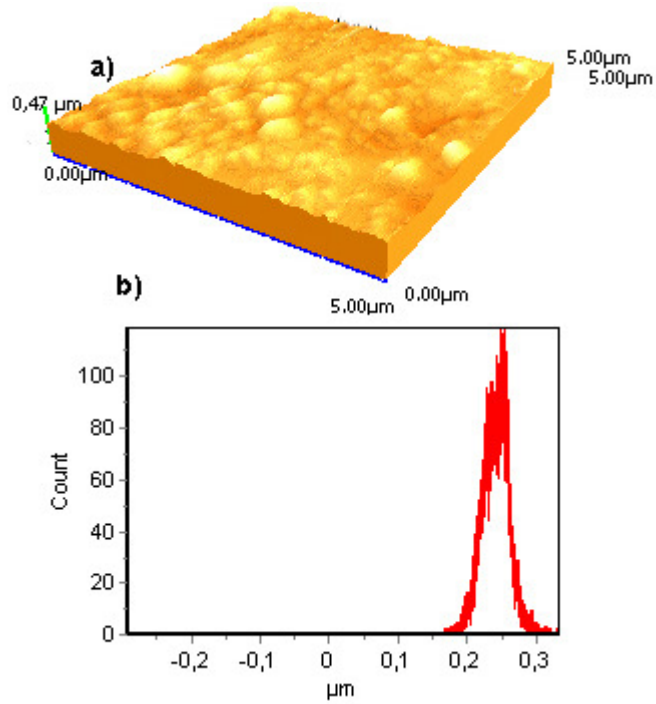Figure 3.23: a) 3D AFM image (5μm x 5μm, 256 x 256 pixels), b) Data histogram, of annealed at 100°C for 45 minutes 90nm Bi thin film
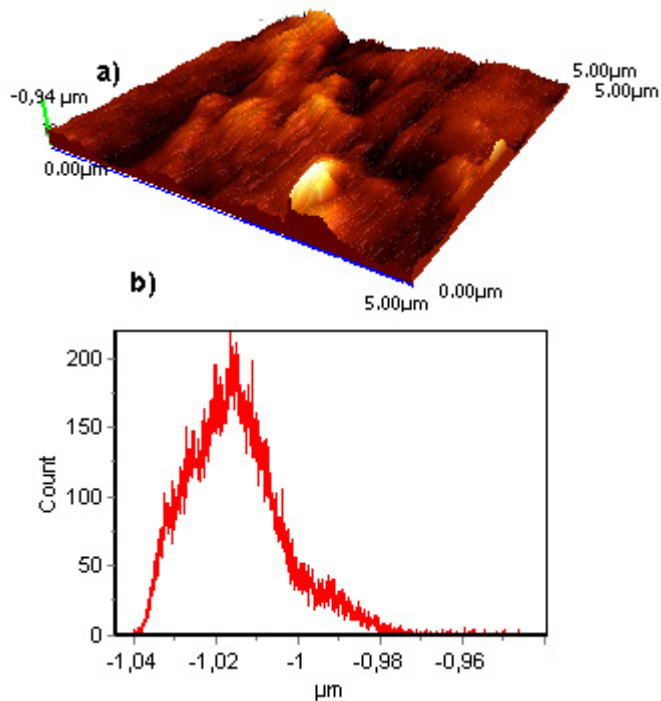
Figure 3.24: a) 3D AFM image (5μm x 5μm, 256 x 256 pixels), b) Data histogram, of annealed at 150°C for 45 minutes 90nm Bi thin film
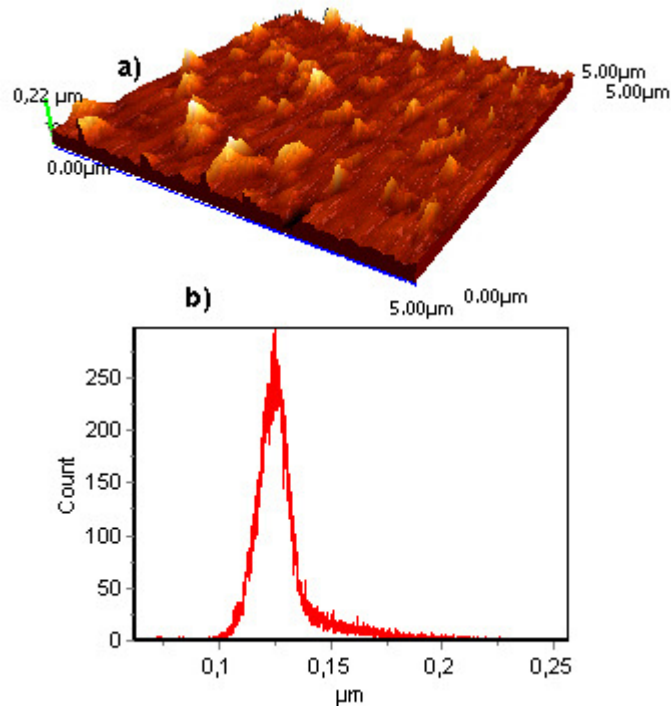
Figure 3.25: a) 3D AFM image (5μm x 5μm, 256 x 256 pixels), b) Data histogram, of oxidized at 150°C for 45 minutes 90nm Bi thin film

It was observed some new features in the AFM image of oxidized 30nm thin film (Fig. 3.11) and that was the indication of oxidization in those films. We conclude this section that the thicker film has been affected by oxidization more so that we expect some bigger features on oxidized 90nm thin film surface. In Fig. 3.25, the sharper and more visible features satisfy us which are compatible with the results of Leontie [27]. To characterize the effect of the oxidization on the surface, we annealed one of two similar samples (grown at the same time) of 90nm thin film under nitrogen gas while the other one annealed under oxygen gas.
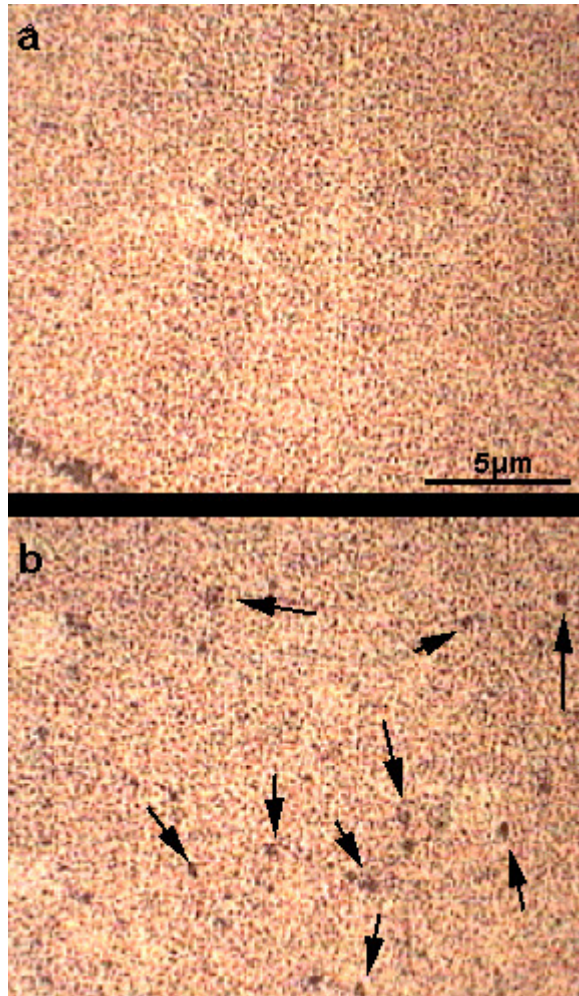
Figure 3.26: a) 20μm x 20μm optical image of 90nm Bi thin film annealed at 150°C for 45 minutes, b) 20μm x 20μm optical image of 90nm Bi thin film annealed under oxygen atmosphere at 150°C for 45 minutes

In Fig. 3.26.a, In the surface which was annealed under inert gas, we observed some small grains in a homogeneous distribution on the surface. However, in the similar sample annealed under oxygen gas, the situation was a bit different. The grains had a homogeneous distribution on the surface however there were some new and bigger features shown by arrows (Fig. 3.26.b). This is a good result to agree with its AFM image (Fig. 3.25). In the AFM image, we observed that the new features on the surface were bigger than the grains as we observed in the optical image.

CHAPTER 4

Conclusions

Bismuth thin film growth by thermal evaporation and its electrical and structural analysis have been described. Our study has shown that Bismuth thin film growth by thermal evaporation is a cheap and fast method for Bismuth studies, however, further studies are needed. Gold contacts are used for the films and have shown ohmic behavior. By those gold contacts, we were able to start the electrical and structural studies without any preannealing process.

The electrical properties of the films have been studied by measuring current-voltage and Hall voltage as function of temperature and fundamental parameters (conductivity, mobility and concentration) have been calculated. By oxidizing those films, we were able to see the resulting effect on the electrical and stuctural properties.

Conductivity is one of the major parameters in electrical characterization. We know that from Eqn.(1.36), we can find activation energy values of the films from conductivity by taking the slope of the curves for different temperature regions. Generally, for both thicknesses of the thin films, the variation in conductivity values as a function of temperature is quite low that is the indication of metallic behavior where the valence and conduction bands are not resolved. We have calculated the activation energy values for the samples. We found that the activation energies were low as a result of metallic behavior of the samples. We observed that oxidization decreased the activation energy values of both samples and also the conductivity of the samples having a thickness of 90nm changed more than that of the 30nm samples by oxidization. We saw that the effect of oxidization was stronger in the thicker film resulting higher carrier concentration and high conductivity. Moreover, the mobility values as a function of temperature give us the scattering mechanisms. In the 30nm samples, we observed that the effective scattering mechanism was lattice scattering in higher temperatures and at lower temperatures impurities started to be dominant. In 90nm film, the mobility

behaviors except oxidized sample did not give any idea about scattering mechanism by means of semiconductor theory (Fig. 3.16). However, for oxidized sample, we may conclude that at respectively higher temperatures, we can see some lattice scattering effects, because the the slope shows a negative value. In this manner, the thicker film showed some degenerate structure so that we loose our chance to discuss its scattering mechanisms.

As a result of structural analysis, it have been observed that all the samples have a polycrystalline phase with small grains. In XRD analysis, it has been investigated the samples have composite Bi_2O_3 (tetragonal) and Bi_2O_3 (monoclinic) structure with the preferred orientation direction in (4 4 2) plane which is the highest peak in the XRD pattern. Our XRD studies have also shown the dependence of the crystal structure to changing temperature. We observed that the increase in the X-ray diffraction pattern was more visible in the temperatures which were higher than the half of the melting point of Bismuth which competed with our AFM results. We observed that thicker film (90nm) required more annealing time to result in a change in the crystal structure. This is an expected result, because there are more atoms in the thicker film to migrate the other grains so that it requires more time to activate the atoms. Therefore, it results in a growing in the grain sizes in the structure of the films that is also reason of increasing intensity of diffraction peaks. After oxidization of the samples, we have observed a decrease in the diffraction peaks showing that the diffusion of the oxides through the bulk has affected the crystallinity of the films. We have also observed from AFM results that the corrugation on the surface has increased by oxidization. So, a decrease in diffraction peaks is a natural result to expect.

To study the surface of Bismuth thin films, a non-contact mode Atomic Force Microscope (nc-AFM) is a successful tool. AFM studies have shown that by annealing the sample, the surface has tried to reach the minimum surface energy level and an annealing temperature which is higher than the half of the melting point of Bismuth has maden the process faster. And the results of the optical microscope of high resolution (x100) have also shown the change in the grain sizes. In AFM study, we have also observed that the thicker film has a smoother surface than that of thinner one just after growth. We know that in thermal evaporation

growth, firstly some clusters occur on the substrate surface which are growing and combining with the each other by continuing evaporation. The number of clusters to combine and to get equilibrium with surroundings will be lower as the process gets longer resulting in a smoother surface. Also, as the film gets thicker, we expect the effect of the substrate topography gets smaller.

In general, we observed the changes on the electrical properties of the Bi thin films by annealing and oxidization. The oxidization did not make us to observe some semiconductor characteristics. We observed some small changes in crystallinity; however, further studies are needed for studying the crystal structure of Bi thin films. We know that growing the samples on hot substrates will result in a sample of higher grain sizes and better crystal structure. Therefore, the thin films can be studied by growing on hot substrates at different substrate temperatures. We also know that magnetoresistance is an important property of Bismuth thin films depending on the crystallinity. Hall effect studies of different thicknesses of Bi thin films at different magnetic fields will be useful to understand the magnetic properties of Bi thin films in oxide form.

REFERENCES

[1] Liang Li, Yong Zhang, Guanghai Li, Lide Zhang, Chemical Physics Letters 378 (2003) 244–249.

[2] F. Y. Yang et al., "Large Magnetoresistance of electrodeposited single-crystal bismuth thin films," Science **284**, 1335-1337 (1999).

[3] S. G. Bompadre, C. Biagini, D. Maslov, and A. F. Hebard, Phys. Rev. B 64, 07310 (2001).

[4] J.H. Mangez, J.P. Issi, J. Heremans, Phys. Rev. B 14 (1976) 4381.

[5] M. Metiko_s-Hukovi_c, Electrochemica Acta 26 (1981) 989.

[6] Münir Dede, M.S. Thesis, 2002, Bilkent University

[7] F. J. Blatt, 1968, *Physics of Electronic Conduction in Solids*, New York: McGraw Hill.

[8] A. C. Smith, J. F. Janak and R. B. Adler, 1968, *Electronic Conduction in Solids*, New York: McGraw Hill.

[9] Omar, M.A. (1993), *Elementary Solid State Physics*, USA: Addison-Wesley Publishers.

[10] R. A. Smith, 1959, *Semiconductors*, Cambridge: Cambridge University Press.

[11] J. S. Blakemore, 1958, *Semiconductor Statistics*, New York: Pergamon Press.

[12] J.P. Issi, Aust. J. Phys. 32 (1979) 585.

[13] Putley, E. H. (1960), *The Hall Effect and Semiconductor Physics*, Toronto: Butterworth&Co. Publishers.

[14] L. L. Kazmerski (1980), Polycrystalline and Amorphous Thin Film Devices, New York: Academic Press.

[15] Flewitt, P. E. J. And Wild, R. K. (1994) *Physical Methods for Microstructural Characterisation of Materials*, Bristol: Institute of Physics Publishing.

[16] Flewitt, P. E. J. And Wild, R. K. (2001), *Grain Boundaries*, England: Wiley Press.

[17] G. Binnig: US Patent 4,724,318 (1986)

[18] Mehrdad Atabak, M.S. Thesis, 2001, Bilkent University.

[19] G. Neubauer, S. R. Cohen, G. M. McClelland, D. Horne and C. Mate, force microscopy with a bidirectional capacitance sensor, Rev. Sci. Instrum.,61, 2296 (1990).

[20] D. Rugar, H. J. Mamin, R. Erlandsson, J. E. Stern and B. D. Terris,Force microscope using a fiber-optic displacement sensor, Rev. Sci. Instrum., 59, 2337, (1988)

[21] D. Rugar, P. Hansma, Atomic Force Microscopy, Physics Today, 11, 23 (1990).

[22] H. Edwards, L. Taylor, W. Duncan, and A. J. Melmed, J. Appl. Phys. 82, 980 ~1997.

[23] G. Meyer, N. M. Amer, Novel Optical approach to atomic force microscopy, Appl. Phys. Lett., 53, 1045 (1988).

[24] QTF RT-AFM, NanoManyetik Bilimsel Cihazlar Ltd., Cyberpark, Cyberplaza, Bilkent, Ankara, Türkiye.

[25] Cryostat, Janis Research Co., Wilmington, MA, USA.

[26] ICDD Cards: 74-2351-C, 76-1730-C.

[27] L. Leontie M. Caraman b, M. Alexe c, C. Harnagea, Surface Science 507–510 (2002) 480–485